

See discussions, stats, and author profiles for this publication at: <https://www.researchgate.net/publication/257412000>


Multi-fingerprint direction and attribution analysis of greenhouse gas, greenhouse gas-plus-aerosol and solar forced climate change

Article in *Climate Dynamics* · December 1997
DOI: 10.1007/s003820050209

CITATIONS
4

READS
25


7 authors, including:



Gabriele C Hegerl
The University of Edinburgh

184 PUBLICATIONS 13,475 CITATIONS


SEE PROFILE



Klaus Hasselmann
Max Planck Institute for Meteorology

188 PUBLICATIONS 18,751 CITATIONS


SEE PROFILE



Ulrich Cubasch
Freie Universität Berlin

272 PUBLICATIONS 10,267 CITATIONS

SEE PROFILE



J. F. B. Mitchell
Met Office


129 PUBLICATIONS 21,023 CITATIONS

SEE PROFILE

Some of the authors of this publication are also working on these related projects:



Interviews with Climate Scientists [View project](#)



DEKLIM EEM: Simulating the Eemian climate with a fully coupled ocean atmosphere circulation model [View project](#)

Multi-fingerprint detection and attribution analysis of greenhouse gas, greenhouse gas-plus-aerosol and solar forced climate change

G. C. Hegerl,^{1*} K. Hasselmann,¹ U. Cubasch,² J. F. B. Mitchell,³ E. Roeckner,¹ R. Voss,² J. Waszkewitz²

¹Max-Planck-Institut für Meteorologie, Hamburg, Germany

²Deutsches Klimarechenzentrum, Hamburg, Germany

³Hadley Centre for Climate Prediction and Research, Bracknell, UK.

Received: 28 April 1996/Accepted: 27 January 1997

Abstract. A multi-fingerprint analysis is applied to the detection and attribution of anthropogenic climate change. While a single fingerprint is optimal for the detection of climate change, further tests of the statistical consistency of the detected climate change signal with model predictions for different candidate forcing mechanisms require the simultaneous application of several fingerprints. Model-predicted climate change signals are derived from three anthropogenic global warming simulations for the period 1880 to 2049 and two simulations forced by estimated changes in solar radiation from 1700 to 1992. In the first global warming simulation, the forcing is by greenhouse gas only, while in the remaining two simulations the direct influence of sulfate aerosols is also included. From the climate change signals of the greenhouse gas only and the average of the two greenhouse gas-plus-aerosol simulations, two optimized fingerprint patterns are derived by weighting the model-predicted climate change patterns towards low-noise directions. The optimized fingerprint patterns are then applied as a filter to the observed near-surface temperature trend patterns, yielding several detection variables. The space-time structure of natural climate variability needed to determine the optimal fingerprint pattern and the resultant signal-to-noise ratio of the detection variable is estimated from several multi-century control simulations with different CGCMs and from instrumental data over the last 136 y. Applying the combined greenhouse gas-plus-aerosol fingerprint in the same way as the greenhouse gas only fingerprint in a previous work, the recent 30-y trends (1966–1995) of annual mean near surface temperature are again found to represent a significant climate change at the 97.5% confidence level. However, using both the greenhouse gas and the combined forcing fingerprints in a two-pattern analysis, a substantially better agreement between observations and the climate model prediction is found for the combined forcing simulation. Anticipating

that the influence of the aerosol forcing is strongest for longer term temperature trends in summer, application of the detection and attribution test to the latest observed 50-y trend pattern of summer temperature yielded statistical consistency with the greenhouse gas-plus-aerosol simulation with respect to both the pattern and amplitude of the signal. In contrast, the observations are inconsistent with the greenhouse-gas only climate change signal at a 95% confidence level for all estimates of climate variability. The observed trend 1943–1992 is furthermore inconsistent with a hypothesized solar radiation change alone at an estimated 90% confidence level. Thus, in contrast to the single pattern analysis, the two pattern analysis is able to discriminate between different forcing hypotheses in the observed climate change signal. The results are subject to uncertainties associated with the forcing history, which is poorly known for the solar and aerosol forcing, the possible omission of other important forcings, and inevitable model errors in the computation of the response to the forcing. Further uncertainties in the estimated significance levels arise from the use of model internal variability simulations and relatively short instrumental observations (after subtraction of an estimated greenhouse gas signal) to estimate the natural climate variability. The resulting confidence limits accordingly vary for different estimates using different variability data. Despite these uncertainties, however, we consider our results sufficiently robust to have some confidence in our finding that the observed climate change is consistent with a combined greenhouse gas and aerosol forcing, but inconsistent with greenhouse gas or solar forcing alone.

1 Introduction

Since the beginning of industrialization, the concentration of greenhouse gases and anthropogenic sulfate aerosols in the atmosphere has continuously increased. There is considerable debate whether the global warming observed during this period can be distinguished from natural

Correspondence to: Gabriele Hegerl

Present address:

*University of Washington, Joint Institute for the Study of the Atmosphere and Ocean, Box 3542 35, Seattle, WA 98195-4235, USA

climate variability and whether the climate change signal, if detected, can be attributed to anthropogenic forcing. Estimates of natural climate variability based on a simple box model (Wigley and Raper 1990) and long simulations with realistic coupled ocean-atmosphere general circulation models (CGCMs; Stouffer et al. 1994) indicate that the observed 100-y trend of global mean temperature is larger than can be explained by the variability of these simulations. Applying information on the space-time structure of the greenhouse gas signal, and the natural climate variability in an optimal fingerprint method, Hegerl et al. (1996) showed that the latest observed 20- and 30-y temperature trend patterns lie above the 95% significance level of current estimates of natural variability. It has been shown by Santer et al. (1995a) that the inclusion of aerosols enhances the agreement between observed and simulated global temperature patterns in summer and autumn and yields statistically significant trends in pattern correlation in these seasons with respect to climate variability estimates from unforced control simulations. The inclusion of aerosols also enhanced the pattern correlation of simulated and observed decadal mean temperature patterns (Mitchell et al. 1995a). A general agreement between observations and simulations has also been found for tropospheric temperature changes (Santer et al. 1996b; Tett et al. 1996). Thus there exists substantial evidence for a forced climate change in the recent decades. A comprehensive summary of the findings of recent pattern-based detection studies is given in the 1995 IPCC Working Group 1 Second Assessment report (Santer et al. 1996a).

Nevertheless, as pointed out in the IPCC report, although a high similarity between observed and simulated patterns suggests that the climate change has indeed been caused by the simulated anthropogenic forcing mechanisms, similar patterns can in principle also be caused by other candidate forcing mechanisms in combination with natural climate variability. Thus the attribution of a detected climate change to a particular forcing mechanism requires the simultaneous consideration of all relevant candidate forcing mechanisms.

To investigate the consistency of the observed climate change with model predictions for different candidate forcing mechanisms we apply here a multi-fingerprint analysis technique. We follow the optimal multi-fingerprint method of Hasselmann (1979, 1993, 1997 which is referred to in the following as Ha97), in which each fingerprint is obtained by rotating the associated signal pattern away from regions of high natural variability towards low noise directions. Santer et al. (1996a) refer to such approaches generally as “stage 3 detection studies”. We note that the optimization is introduced in our case to maximize the signal-to-noise ratio in estimating the contribution from different climate change signals to the observations, but is not a prerequisite of the attribution approach as such.

As observed climate data we use the near-surface temperature data set of Jones and Briffa (1992). We apply a simplified form of the general space-time dependent optimal fingerprint method of Hasselmann (1993, Ha97) in which the rotation of the signal guess-patterns is carried out with respect to the spatial coordinates only, rather than in full space-time. The signal patterns are obtained

from simulations with coupled ocean-atmosphere general circulation models (CGCMs). A basically similar approach has recently been applied to the space time evolution of near surface temperature, using 7–17 y band-passed data and climate change signals derived from time-dependent energy balance model simulations (North and Stevens, 1998). Their results are consistent with ours. Here we use multi-decadal linear trends to describe the time-evolution of the climate change signal. We analyze time intervals of 50 y or shorter, since for such intervals the relevant level of natural variability can be estimated with higher confidence from model control simulations and even, to some extent, from observations. By focusing on shorter time intervals we also make use of the fact that most transient CGCM simulations yield a marked enhancement of the warming rate in recent decades (Hasselmann et al. 1995; Cubasch et al. 1995; Mitchell et al. 1995a) which is associated with the increase in the forcing and a warming delay due to the heat uptake by the oceans. An optimal trend interval for exploiting the predicted warming acceleration is about 30 y. However, somewhat longer trends, e.g. over 50 y, are more efficient at distinguishing a sulfate aerosol signal from the background noise, since the global mean sulfate burden has been increasing nearly linearly over the last 40 to 50 y (see also Santer et al. 1996b).

An additional forcing which may have influenced the observed temperature record in the relevant detection time scale range of a few decades to a century is a variation in solar insolation. Estimates of such variations have been derived by Hoyt and Schatten (1993) and Lean et al. (1995). Since the estimates suggest a relatively minor increase in solar radiation over the previous 50 y, whereas both anthropogenic forcing factors have been strongly increasing in the same period, 50-y temperature trends might provide also a good discriminator between solar and anthropogenic forced variations.

Thus, we consider three climate change signals, which we derive from simulations forced with greenhouse gases alone, greenhouse gases plus aerosols, and changes in solar radiation (Cubasch et al. 1996; 1997). A single-fingerprint detection analysis using the combined greenhouse gas-plus-aerosol signal, applied to observed 30-y temperature trend patterns yields results very similar to the earlier positive detection results of Hegerl et al. (1996, referred to in the following as Hetal96) using a greenhouse gas only fingerprint. The similarities in the results, despite differences in the forcing patterns, can be explained by the fact that for a single fingerprint the response is dominated by the global mean temperature increase, and is relatively insensitive to spatial details of the pattern (Santer et al. 1993; 1995a; Hetal96). However, if a multi-pattern optimal fingerprint method is applied, differences in the pattern details become important, and we find that the observations are no longer consistent with greenhouse gas forced climate change alone. They are also found to be inconsistent (at a lower significance level) with solar forced climate change alone. However, they remain consistent with a combined greenhouse gas-plus-aerosol forcing.

We use only two fingerprint patterns for our analysis, one for the greenhouse warming and one for the additional, statistically orthogonal pattern representing the

aerosol forcing. We have not introduced a third fingerprint pattern representing the response to solar variations, since it was not possible to reliably separate the response pattern for this relatively small forcing from the overlying climate variability noise over parts of the planet (Cubasch et al. 1997; see Sect. 2.3). Thus, we represent the solar forcing signal as a time dependent linear combination of the two response patterns for anthropogenic forcing.

The attribution of climate change to a given cause is subject to more uncertainties than the detection of climate change (Santer et al. 1996a). The candidate mechanisms need to be specified, together with the magnitude of the forcing and the magnitude and pattern of the response. As pointed out in Hetal96 and Ha97, for detection, the predicted amplitudes of the forcing and response are irrelevant, and the predicted climate change patterns need not be correct. An incorrect pattern reduces the power of the detection test, possibly preventing detection, but will not normally lead to false detection claims. However, for attribution, incorrect forcing and model errors producing incorrect response predictions result in an incorrect assessment of the consistency between climate change simulations and observations, and can lead either to a failure to recognize a response signal or to an unjustified attribution claim. In this context we note that in the case of solar and sulfate aerosol forcing, there is still high uncertainty regarding the magnitude and pattern of the forcing, in addition to inevitable errors in the models themselves. In principle, the impact of model errors can be incorporated in the attribution analysis (Ha97). However, this has not been attempted in the present study, since the relevant model error covariance matrix for decadal trends is difficult to estimate. Further uncertainties, which affect in this case both the detection and attribution analysis, are associated with the estimate of natural climate variability from model simulations and observational time series of limited extent.

Another limitation of both the detection and attribution method is the basic assumption that different forcing mechanisms can be superimposed linearly without interacting with each other and with the natural climate variability. This is essential for our method of separating the contributions from natural variability and different combinations of forcing. Fortunately, there are indications that this is an acceptable approximation, at least for the greenhouse gas and aerosol forcing response (Santer et al. 1995).

The work is structured as follows: Sect. 2 outlines the optimal fingerprint method for detection and attribution of climate change. In Sect. 3, some results of the climate model simulations are shown and the data used for applying the detection and attribution approach are specified. Results for annual mean data are given in Sect. 4 and 5, using one or two fingerprints, respectively. A similar analysis for seasonally stratified data is presented in Sect. 6, where we test also the consistency of the observed climate change with each of the hypothesized forcing mechanisms. We conclude with a summary and discussion of the results in Sect. 7. A summary of the various steps involved in the optimal multi-pattern method and further technical details are given in the Appendix.

2 The optimal fingerprint method for detection and attribution

Various pattern analysis methods have been proposed which make use of the model-predicted patterns of anthropogenic (or other externally forced) climate change to distinguish the forced signal from natural climate variability (noise) (see reviews in Barnett et al. 1991; 1994). The optimal fingerprint method (Hasselmann et al. 1979; 1993) adopted here is based on an enhancement of features of the climate change signal associated with low natural variability relative to features which are more strongly contaminated by noise. Such techniques which maximize the signal-to-noise ratio are considerably more powerful than the selection of arbitrary climate indices (e.g. the global mean temperature) as detection variable, but require knowledge of the space-time structures of both the signal and the noise. This approach is useful not only for the early detection of externally forced climate change, but also to distinguish between different candidate forcing mechanisms in the attribution problem (Ha97). The optimal fingerprint method has been applied by Santer et al. (1995b) for the detection of ocean global warming in a model simulation study and by Hetal96 for the detection of a greenhouse warming signal in near surface temperature data. It can be shown that the optimal fingerprint method is closely related to other optimal averaging or filtering methods (Bell 1986; North et al. 1995; see Hegerl and North 1997) which provide an optimal estimate of the amplitude of a climate change signal in the presence of noise, and to similar approaches which have been used in other fields of signal processing (see Hasselmann 1979; Allen and Tett 1997).

2.1 Optimal fingerprints

Observations of recent climate evolution may contain several climate change signals, e.g. through greenhouse warming, increasing aerosol concentrations, or changes in solar radiation. To distinguish between different candidate mechanisms, it is useful to introduce several fingerprints f_v , $v = 1 \dots p$ associated with the different signal guess-patterns g_v predicted for the different forcings, and to consider a vector of detection variables defined by the scalar products (Hasselmann 1993, Ha97)

$$d_v = \sum_i \underline{f}_v^i \Psi_i = \underline{f}^T \Psi, v = 1 \dots p \quad (1)$$

where $\underline{\Psi} = (\Psi_i)_{i=1 \dots n}$ represents the observed climate state vector (in some n -dimensional, e.g. gridpoint, space). Underlines indicate climate vectors, a superscript “ T ” the transposed vector. The optimal fingerprints are defined such that they maximize the square signal-to-noise ratio for each individual signal component. This yields at the same time the maximal multi-variate signal-to-noise ratio for the combined multi-pattern signal. For optimal detection (disregarding the question of attribution) the restriction to a single fingerprint generally yields the highest signal-to-noise ratio, since the significance of a given climate change signal decreases with increasing dimension (e.g. Ha97). The optimal fingerprints are given by the

product of the original signal guess-pattern with the inverse C^{-1} of the covariance matrix $(C_{ij})_{i,j=1\dots n} = \langle \tilde{\Psi}_i \tilde{\Psi}_k \rangle$ of the random climate noise $\tilde{\Psi}$,

$$\underline{f}_v = C^{-1} \underline{g}_v. \quad (2)$$

where the cornered brackets denote the statistical expectation. The covariance matrix can be estimated using samples of model-derived or observed climate noise (see later). The multiplication with the inverse covariance matrix suppresses features of the signal pattern associated with high natural variability and enhances pattern features for which the variability is low. This is seen most readily in the EOF representation $C = \text{diag}(\sigma_i^2)_{i=1\dots n}$, for which the fingerprint is obtained by simply dividing the EOF coefficients of the signal pattern by the variance of climate noise σ_i^2 .

Equations (1) and (2) show that the application of an optimal fingerprint can be understood as regressing the observations upon the model signal pattern using a scalar product (and metric) which takes the noise in the variable components, as represented by C^{-1} , into account. A more elegant representation is to understand the fingerprint \underline{f}_v^i as the contravariant dual vector of the covariant signal pattern vector \underline{g}_{vi} (Hasselmann 1979; Ha97).

The normalization of the individual signal patterns and associated fingerprints is basically arbitrary. We shall normalize the signal patterns such that

$$\underline{g}_v^T C^{-1} \underline{g}_v = 1 \quad (3)$$

which implies for the fingerprints, according to Eq. (2),

$$\underline{f}_v^T C \underline{f}_v = 1. \quad (4)$$

We cannot impose orthonormality of the original signal patterns, since these are specified as the response to different forcings, which in general will not be orthogonal. However, we shall nevertheless find it convenient later to transform to an orthonormal set of signal patterns and fingerprints, consisting of linear combinations of the original signal patterns and fingerprints, for which

$$\begin{aligned} \underline{g}_v^T C^{-1} \underline{g}_\mu &= \delta_{v\mu} \\ \underline{f}_v^T C \underline{f}_\mu &= \delta_{v\mu}. \end{aligned} \quad (5)$$

Detection is said to be achieved at some prescribed significance level P (e.g. 95%) if the “null” hypothesis that the observed detection variable d (or vector of detection variables) can be explained by natural variability alone is rejected at that significance level, i.e. if the probability that a signal of at least the estimated magnitude is sampled from the natural variability ensemble lies below the level $1 - P$ (e.g. 5%). Here, as in the subsequent treatment of the attribution problem, we adopt a conventional non-Bayesian approach, in which probabilities are introduced only with respect to an ensemble of realizations (or when such an ensemble can be constructed from statistically stationary time series). From a Bayesian viewpoint it can be argued that the rejection of the null hypothesis at some prescribed significance level, implying the acceptance of the alternative hypothesis of an externally forced climate change, cannot be meaningfully formulated without

specifying the prior probability of the alternative hypothesis. However, since there exists no statistical basis for the determination of this probability, it can be expressed only as a subjective “degree of belief” (see Earman 1992). Prefer to remain within the less controversial confines of conventional non-Bayesian statistics, a pilot application of Bayesian detection is attempted in Leroy (1997).

2.2 Application of multiple optimal fingerprints to the attribution problem

The rejection of the null hypothesis in the detection test implies only that the magnitude of the detection variable, defined with respect to some assumed signal direction, is too large to be explained by natural variability. It does not address the question whether the observations are in fact consistent with the model predicted signal, or with other model simulations using different forcing hypothesis (e.g. greenhouse gases alone, greenhouse gases plus aerosols, solar insolation changes, and so forth). This is the essence of the attribution problem.

To test the consistency of a detected climate change signal with the signal predicted by a model we need to represent the observed climate change signal in terms of the model signal patterns \underline{g}_v , $v = 1, 2, \dots, p$:

$$\underline{\Psi} = \sum_{v=1}^p a^v \underline{g}_v + \tilde{\Psi}^r. \quad (6)$$

where $\tilde{\Psi}^r$ is a residual. If the response to all external forcing has been properly represented by the signal patterns, $\tilde{\Psi}^r$ will consist of climate noise only. The estimated signal pattern amplitudes a^v will consist generally of linear combinations of the detection variables d_v and can be computed by a multi-pattern regression using the metric C^{-1} . Thus, the p -dimensional amplitude vector $\mathbf{a} = (a^v)_{v=1\dots p}$ is obtained from the condition that the mean square residual $\tilde{\Psi}^r$ (defined in terms of the metric C^{-1}) is minimized:

$$\tilde{\Psi}^{rT} C^{-1} \tilde{\Psi}^r = \min \quad (7)$$

This least square fit yields (Ha97)

$$\sum_v G_{v\mu} a^v = \underline{g}_\mu^T C^{-1} \underline{\Psi} = d_\mu \quad (8)$$

where

$$G_{v\mu} = \underline{g}_v^T C^{-1} \underline{g}_\mu. \quad (9)$$

If the signal patterns are statistically orthonormal relative to the noise covariance matrix (Eq. 5), $G_{v\mu}$ is the unit matrix $G_{v\mu} = \text{diag}(1)$. The detection variable components are then statistically uncorrelated and yield the amplitude estimate directly: $a^v = d_v$.

(For a consistent invariant tensor notation for the dual co- and contravariant detection and amplitude variables d_v and a^v , respectively, using the metric $G_{v\mu}$, we refer to Ha97.)

2.3 Estimation of confidence intervals for the attribution test

For the attribution test, we intercompare the predicted and observed signal vectors $\mathbf{a} = (a^v)_{v=1 \dots p}$ specifying the amplitudes of the climate change patterns g_v (vectors in the p -dimensional detection variable space are printed bold). To assess the statistical significance of deviations between the two amplitude vectors, we need to determine the uncertainties in both signals.

The uncertainty of the model predicted climate change signal consists generally of two contributions:

1. The uncertainty associated with the estimate of the climate change signal derived from a single or a small number of model simulations which are contaminated by model-generated climate variability.
2. The uncertainty associated with systematic model errors, ideally characterized by some model error covariance matrix. For the signal patterns used in this study, the uncertainties are discussed in Sect. 3. The errors are difficult to estimate quantitatively, and we shall therefore not include them in our statistical test. However, they need to be kept in mind when interpreting the results.

In principle, the first uncertainty can be removed by carrying out a large number of simulations, starting from different initial conditions, and forming the ensemble average (Cubasch et al. 1994). However, an adequate noise reduction is often not feasible due to computer time limitations (note that N simulations reduce the rms uncertainty only by \sqrt{N}). Thus, the imperfect model estimated climate change signal will differ from the “true” (unknown) model predicted climate change signal $\mathbf{a}_M = (a_M^v)_{v=1 \dots p}$ by a sampling error governed by the statistics of the model’s internal variability. In the following we assume that the superimposed climate variability is Gaussian, although an approach similar to the one discussed later can also be performed for other statistics. Then, the model climate change signal derived from a single simulation \mathbf{y} represents a realization from a Gaussian distribution $\mathbf{y} \sim N(\mathbf{a}_M, \Sigma_M)$ where Σ_M denotes the model noise covariance matrix in the p -dimensional space spanned by the different climate change signals. Note that the signal uncertainty will also extend into the remaining dimensions of the climate phase space, but these dimensions are irrelevant for the problem of distinguishing between a given finite set of p candidate forcing mechanisms. Since we assume that the noise is superimposed linearly on the climate change signal, Σ_M can be inferred from the variations in the signal estimate due to noise only, which can be computed from a long control simulation using the same climate model. If \mathbf{y} is computed from the average of N different simulations, Σ_M is reduced by the factor $1/N$.

Similarly, the climate change signal estimated from the observations will deviate from the “true” underlying climate change signal $\mathbf{a}_{obs} = (a_{obs}^v)_{v=1 \dots p}$ through the superimposed internal variability of the climate system. The signal vector inferred from the observations \mathbf{x} will then also originate from a normal distribution $\mathbf{x} \sim N(\mathbf{a}_{obs}, \Sigma_{obs})$. If the climate model simulates the internal

variability noise correctly, and all relevant forcings were considered, the uncertainty associated with a single model simulation Σ_M would equal Σ_{obs} . However, this is not exactly the case, as will be discussed further in Sect. 5.

Both uncertainties enter in the attribution test, in which we consider now the statistical significance of the difference vector $\mathbf{x} - \mathbf{y}$: We make the hypothesis that the model predicted climate change signal (or combination of signals) is correct. In this case $\mathbf{a}_{obs} = \mathbf{a}_M$, and the probability distribution of the difference vector $\mathbf{x} - \mathbf{y}$ between the observations \mathbf{x} and model simulation \mathbf{y} is given by the normal distribution

$$\mathbf{x} - \mathbf{y} \sim N(0, \Sigma_{obs} + \Sigma_M) = N(0, \Sigma), \quad \mathbf{x} \sim N(\mathbf{y}, \Sigma). \quad (10)$$

where we have set $\Sigma = \Sigma_{obs} + \Sigma_M$, since the noise realizations of the model and the observations are independent. From the distribution Eq. (10) we can define ellipsoids of constant probability density containing, say, 90% of the realizations of the difference vector $\mathbf{x} - \mathbf{y}$ (von Storch and Zwiers in preparation 1997). If the model simulated climate change signal disagrees significantly from the observations, i.e. if the observations are not contained in the 90% uncertainty ellipsoid, the associated forcing mechanism is rejected as a plausible cause for the observed climate change signal at the 90% confidence level. Conversely, if the difference vector $\mathbf{x} - \mathbf{y}$ lies within this ellipsoid, the observations are considered to be statistically consistent with the postulated forcing mechanism, or sum of forcing mechanisms. A more rigorous terminology would be to say in this case that the observations are not inconsistent with the postulated forcing. However, we shall use the simpler but less precise direct wording.

3 Components of the detection and attribution approach

We describe in the following the basic ingredients of our multi-pattern detection and attribution analysis: the observed data; the model simulations forced with greenhouse gases, greenhouse gases plus aerosols, and varying solar insolation; the signal-guess patterns derived from the global warming simulations; and the data for natural climate variability. We focus here on annual mean values: the generalization to seasonal values is described in Sect. 6.

3.1 Observations

The observed near-surface temperature data used for the multi-fingerprint approach have been compiled as anomalies (with respect to the average of the years 1950–1979) of monthly mean near surface temperature on a $5^\circ \times 5^\circ$ global grid by Jones and Briffa (1992) and Jones (1994 a, b). The data range from the year 1854 to 1995, with data coverage changing in time. Global-mean near-surface temperature curves and the decadal mean pattern of temperature change based on these data are presented in the Supplementary Report to the IPCC Working Group 1 Scientific Assessment (Folland et al. 1992). As in Hetal96, annual mean values at a gridbox were computed

if at least one seasonal mean (computed from at least one month) was available, otherwise the annual mean was indicated as missing. This criterion allows a relatively high spatial coverage, but may introduce some additional noise. It corresponds to a similar criterion applied to the computation of decadal mean patterns in Folland et al. (1992). Our results were found to be insensitive to the criterion (e.g. use of a stricter acceptance condition of at least three seasonal means for an annual average). We also made a sensitivity test applying the newer, updated dataset used in IPCC 1995 (Nicholls et al. 1996; Parker et al. 1994). This yielded some difference in the results, but without affecting our basic conclusions. In the computation of averages of simulated and observed data as well as in the subsequent multi-fingerprint analysis, we considered only gridpoints for which the observations enable the computation of multi-decadal trends after 1949 with no than one missing year between any two years with data. This yields approximately 75% global coverage for annual mean data (see Fig. 3). 30-y trend patterns computed in this manner are shown in Hetal96.

3.2 Climate change simulations

The temperature change patterns for greenhouse gas only and combined greenhouse gas-plus-aerosol forcing are derived from five climate change simulations with the coupled ocean atmosphere model ECHAM3 + LSG, in the following referred to as HAM3L (Hasselmann et al. 1995; Voss et al. submitted 1997). The model is a new version of the Hamburg CGCM (Cubasch et al. 1992; Maier-Reimer et al. 1993; Roeckner et al. 1992) using an updated atmosphere model (ECHAM3) at a spectral T21 resolution. Three anthropogenic climate change experiments start with forcing conditions of the year 1880 and are continued up to the year 2049. Two simulations (A and B) were carried out for a combination of both greenhouse gas forcing and the direct (albedo) effect of sulfate aerosols, while in the third simulation (C), only the greenhouse gas forcing was considered. The two greenhouse gas-plus-aerosol simulations differ only through the introduction of a small perturbation (at least an order of magnitude smaller than the uncertainty in the aerosol forcing, see Penner et al. 1995) into the aerosol fields of one of the runs. Using more than one simulation enables a better separation of the climate change signal from the internal climate variability (as discussed above, and is evident from the independent fluctuations of the two simulations).

The greenhouse gas concentrations were expressed in terms of net equivalent CO₂ concentrations (Houghton et al. 1990). From 1880 to the present these were reconstructed from direct measurements since 1957 and, prior to that date, from estimates derived from ice cores (Schönwiese et al. 1990; Houghton et al. 1990). For the future, the IPCC Scenario A data were used (Houghton et al. 1990). The sulphate aerosol data were kindly made available by the Meteorological Institute of the Stockholm University and were calculated using the MOGUNTIA sulphur model (Langner and Rohde 1991) from historical SO₂ emissions, based essentially on Mylona (1993) and

Gschwandtner et al. (1986), and from projected future emissions from the IPCC 1992 scenario A (Pepper et al. 1992).

The scenario forcing fields are similar to those shown in Mitchell et al. (1995a, b), except that the pattern of the aerosol forcing was not spatially fixed before 1990, but was allowed to respond to the spatially changing patterns of sulfur emissions (see Mitchell and Johns 1997). The forcing fields are shown in Cubasch et al. (1996). The impact of the computed aerosol concentrations was represented in the CGCM as an increased effective surface albedo. The global mean of the radiative forcing at the top of the atmosphere due to the aerosols is approximately -0.7 W/m^2 in 1980. Indirect effects of aerosols on the formation and radiative properties of clouds were not considered. These are generally estimated to be of comparable magnitude to the direct effects, and may produce different climate change patterns (Jones et al. 1994; Boucher and Lohmann 1995). Our computations of the aerosol climate impact must therefore be regarded as only qualitative.

We furthermore use two simulations (SOL1 and SOL2), starting from different states of the control simulation, forced with estimated solar radiation variations between 1700 and 1992 after Hoyt and Schatten (1993). A slightly different index of solar variations has been proposed by Lean et al. (1995), see Crowley and Kim (1996). The simulations are described in Cubasch et al. (1997). Estimates of solar radiation variations are highly uncertain and controversial, so that the results of these simulations must also be regarded with caution.

Figure 1 shows the time evolution of the average over the analysis area (covered by observations) of near surface temperature of the observations and the simulations for the three forcing cases. The two pairs of greenhouse gas-plus-aerosol simulations A and B and solar forcing experiments SOL1 and SOL2 were averaged, while the greenhouse gas only case was represented by a single experiment C. All temperature change patterns are computed relative to the mean over the reference period 1950–1979. The residual drift of the control simulation may have slightly influenced the time evolution of the anthropogenic climate change experiments (see later), especially in the early part of the simulation.

The two curves from the anthropogenic climate change simulations follow each other rather closely until about 1975. From 1975 onwards, the influence of the aerosols becomes noticeable, the greenhouse gas only experiment C showing a temperature rise of about 0.3 K per decade, compared to 0.2 K per decade for the mean of the aerosol experiments A and B. The mean of the simulations with varying solar forcing shows some rise in global mean temperature over the period 1880 to 1992. The visual impression of Fig. 1 is that it is hard to distinguish which of the different forcing hypotheses agrees best with the observations on the basis of global mean temperature alone.

Figure 2 shows the regional distribution of annual mean changes in northern hemispheric temperature for the simulations (a) without and (b) with inclusion of the aerosol forcing. The aerosols show the largest effects in the Northern Hemisphere, where the main sources of the

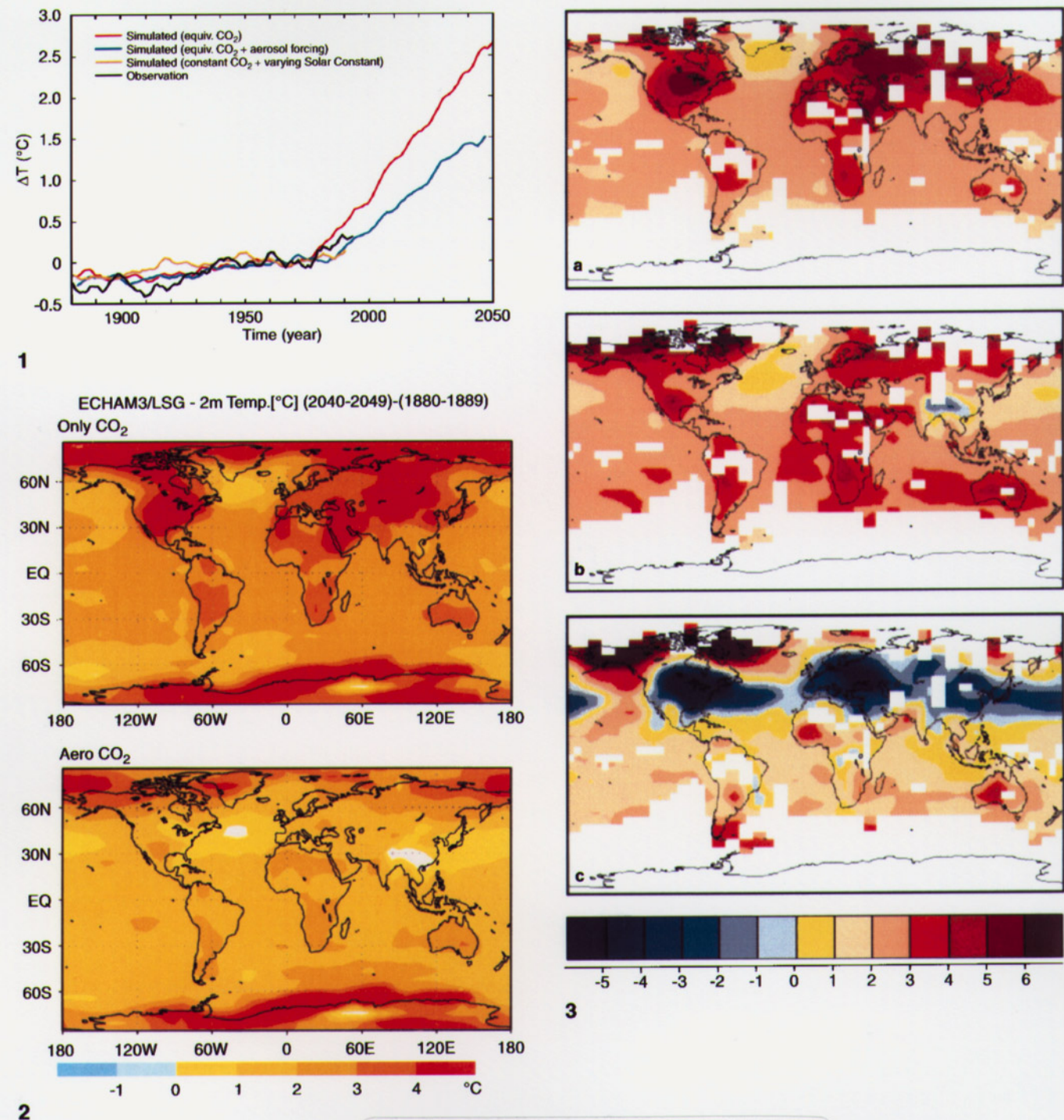


Fig. 1. Time evolution of global mean near surface air temperature from climate model simulations compared with observations (5-y running mean). The model simulations are driven with greenhouse gas forcing only (simulation C), greenhouse gas-plus-aerosol forcing (experiments A, B, averaged in the figure) and estimated variations in solar radiation (simulations SOL1, SOL2, similarly averaged). Temperature changes are defined relative to the mean of years 1950–1979 and are averaged only over areas used for the detection analysis for which a sufficient number of observations is available (see Fig. 3)

Fig. 2. Change of annual mean near surface air temperature (in $^{\circ}\text{C}$) in the mean over the decade 2040–2049 relative to the initial decade of the simulations (1880–1889) for the greenhouse gas only experiment C (top) and the average of (A + B)/2 of the two experiments with greenhouse gas-plus-aerosol forcing (bottom)

Fig. 3a–c. Dominant annual mean climate change signal (first EOF) for **a** greenhouse gas only forcing and **b** the average (A + B)/2 of the two combined greenhouse gas-plus-aerosol forcing experiments (normalized to same mean square deviation). The patterns are restricted to grid-points for which reliable trends could be calculated since 1949 from the observations. **c** Shows the greenhouse gas-plus-aerosol pattern after orthogonalization (using the metric given by the inverse noise covariance matrix, Eq. 5) with respect to the greenhouse gas only signal pattern. This represents the additional, statistically independent climate change pattern associated with the aerosol forcing

anthropogenic sulphate aerosols are located. This hemisphere also shows the strongest seasonal signal (Cubasch et al. 1996). The impact of the aerosol forcing is largest in summer and in low-and mid-latitudes, where the albedo effect is more effective due to the stronger insulation.

3.3 Signal patterns of the model predicted climate change

As mentioned, we use two signal patterns g_v and associated fingerprints f_v for the detection and attribution analysis: one for the greenhouse gas only signal g_c and one for the combined greenhouse gas-plus-aerosol signal g_{ab} . It would have been desirable to complete the signal pattern set by using also a third pattern representing the response to variations in solar forcing. Cubasch et al. (1997) did in fact derive a solar forcing response pattern by performing a regression of the solar forcing time series onto the surface temperature model response, which could, however, not be reliably separated from the overlying climate variability noise over parts of the planet (Cubasch et al. 1997). The authors found a strong resemblance of that pattern to the greenhouse warming pattern, the physical mechanism of the pattern differences could not be clearly established due to superimposed noise. Since previous tests showed that the results using optimal fingerprints tend to deteriorate rapidly for strongly noise contaminated signals, we prefer to analyze the solar forcing response here in the pattern space spanned by our two anthropogenic response signals. A discrimination between the response to solar and greenhouse gas forcing using both response patterns (using Euclidean rather than optimal metric), was attempted in Cubasch et al. (1997). The results showed that the recent observed temperature trends resemble rather the greenhouse warming pattern than the solar response pattern.

In the case of greenhouse gas forcing, it was shown by Cubasch et al. (1992) that the first EOF (empirical orthogonal function) captures most of the model response. Accordingly, we define the temperature change patterns for both anthropogenic forcing cases as the first EOFs of the model response. We used the full length of the time series to compute the EOFs rather than the response only up to the present time, since in the latter case the response (as computed from only one or two simulations) was still relatively small and was contaminated by climate variability noise. Defining the signal patterns in terms of the EOFs proved to be a more stable choice in the present case than the previous definition of Hetal96 in terms of the difference between the last and an early decade of the simulation.

This applies particularly for the combined forcing simulations, for which the climate change signal is smaller than for the greenhouse gas only simulation, while for the greenhouse gas only signal the difference between the two definitions is relatively minor. As in our previous definition of the global mean temperatures, the EOFs are computed from anomalies relative to the average over the model years 1950–1979 (i.e. relative to the reference period used in the observations) and only over areas with sufficient observational coverage. This ensures that the EOFs focus on the variance in the same areas which are used later for detection.

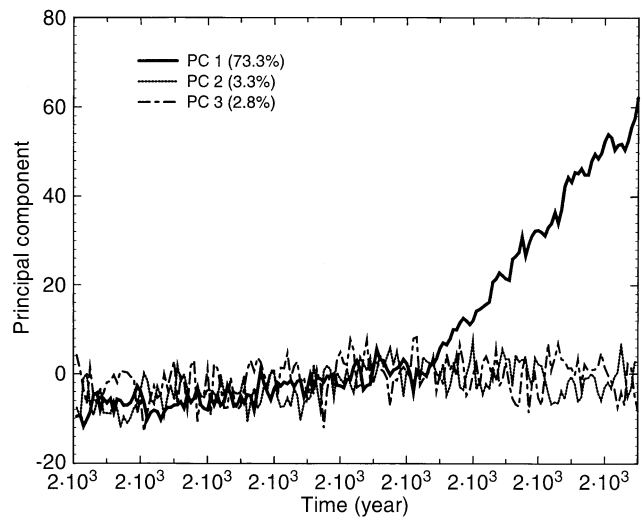


Fig. 4. Time evolution of the first 3 EOFs of the mean of the two greenhouse gas-plus-aerosol forcing simulations. The first EOF captures most of the increasing climate change signal, while higher EOFs contain mainly noise

The first EOF of simulation C yields a very stable representation of the annual mean climate change signal, explaining about 90% of the time evolution (Fig. 3a). To enhance the signal-to-noise ratio, the signal pattern (Fig. 3b) for the greenhouse gas-plus-aerosol simulations A, B was determined from the first EOF of the mean of both simulations $(A + B)/2$. The signal pattern is rather similar to the greenhouse gas climate change signal except in the northern mid-latitudes, where the warming is reduced due to the aerosol effect. The full signal pattern correlation (including the spatial mean) between the EOFs of simulations $(A + B)/2$ and C is $r^* = 0.93$, while the reduced (“centered”; Santer et al. 1993) correlation, after subtraction of the spatial mean, is $r = 0.32$.

As in greenhouse gas only simulations the first EOF of the mean $(A + B)/2$ of both greenhouse gas-plus-aerosol forcing simulations captures most of the time-evolution of the combined greenhouse gas-plus-aerosol climate change signal (Fig. 4). It explains 73% of the variance of the averaged simulation (compared to 59% for the single simulation A). The remaining EOFs show no systematic trends in the model years after about 1980 and have the appearance of noise. This result is confirmed by the computed 30-y trends of the principal components (not shown). Nevertheless, in the case of the greenhouse gas-plus-aerosol simulation, where the spatial distribution of the aerosol forcing varies in time, some spatial details of the predicted present-day climate change pattern are presumably distorted through the use of the first EOF of the entire simulation as time invariant signal pattern. Thus the strong cooling over China in the first EOF, Fig. 2, 3b, is governed largely by the strong increase in aerosol forcing predicted in the IPCC scenario for the next century. Unfortunately, a more reliable computation of the present climate change signal would require a larger number of climate change simulations than is presently feasible.

Some uncertainty is introduced by a drift in the HAM3L model. The drift appears to originate in the ice-edge area of the Southern Hemisphere and causes a global mean warming of approximately 0.5°C in the first 160 y of the simulation. Since we have computed the climate change pattern relative to a constant mean state (the average over the model years 1950–79), the slow warming trends especially in the first half of this century (Fig. 1) in the anomaly simulations A, B and C, and thereby also the signal pattern, could be influenced by a common model drift. However, the area in which the strongest drift occurs, the high southern latitudes, are not included in our signal guess-pattern (see Fig. 3). In order to qualitatively assess the effect of drift, we have also computed the first EOF of the climate change simulation defined relative to the contemporaneous state of the control simulation (i.e. by subtracting CTL year by year from the climate change simulations, see discussion in Cubasch et al. 1992). The resulting time evolution of the first principal components after the model year 1970 is very similar in both cases. The first EOFs are also very similar, with a centered pattern correlation of $r = 0.97$. The differences between the patterns (not shown) have the appearance of climate variability noise. We have used our original signal pattern definition, since subtracting the control simulation introduces additional noise.

The Hadley Center simulations (Johns et al. 1997; Mitchell and Johns 1997; Mitchell et al. 1995a,b; Kattenberg et al. 1996) yield similar rates of temperature increase to ours, both with and without aerosols, and quite similar spatial patterns. However, the responses to the two forcings separate about 20 y earlier in the Hadley Centre simulations. The climate change pattern of our new greenhouse warming simulation C shows a different pattern of warming over Europe and more pronounced warming over parts of the Northern Hemisphere mid-latitude land masses than previous simulations using an earlier version of the Hamburg climate model (Cubasch et al. 1992; 1994a,b). This may be attributed to a more realistic circulation, especially over the North Atlantic, in the updated atmosphere model ECHAM3 (Roeckner et al. 1992). However, the differences between the climate change signal of simulation C and the climate change signals of the earlier simulations (characterized by a centred signal pattern correlation of $r = 0.47$ for the EIN simulation of Cubasch et al. 1994b, and $r = 0.64$ for the scenario A simulation of Cubasch et al. 1992) are still substantially smaller than the differences with respect to the combined greenhouse gas and aerosol simulation.

In summary, there are uncertainties of the signal pattern associated with the initial residual drift of the control simulation, possible errors in the model response, the definition of the present-day response from the first EOF of the entire simulation, and the inadequate removal of the natural variability noise achievable with a single greenhouse gas only simulation C and two greenhouse gas-plus-aerosol simulations (Cubasch et al. 1994). Still larger uncertainties arise from our present insufficient knowledge of the sulfate concentrations and, in particular, the resulting forcing (e.g. we have disregarded indirect aerosol forcing). We have also ignored other possible mechanisms of externally forced climate change, such as changes in

ozone concentration, non-sulfate aerosols and land-surface changes. These shortcomings must be kept in mind in our later discussion of the attribution problem.

3.4 Natural climate variability

Estimates of the space-time structure of the natural near-surface temperature variability are needed for two purposes: to estimate the noise covariance matrix (Eq. 2) for the computation of the optimal fingerprint; and to estimate the variability of the detection variable in order to compute significance levels for climate change detection and confidence ellipses for attribution. We use both model data and observations to estimate the natural variability.

Our model data consists of four CGCM simulations of the present climate over several centuries: 1000 y from a simulation with the model ECHAM/LSG, referred in the following as HAML (von Storch 1994; von Storch et al. 1997), a 1000 y simulation with the GFDL model (Manabe and Stouffer 1993, 1996), 700 years with the model HAM3L, which has also been used for the climate change simulations, and 611 annual means from the control simulation with the HADCM2 model (Mitchell et al. 1995a; Johns et al. 1997; Tett et al. 1997). HAML has been used for a number of climate change simulations previously and is described in Cubasch et al. (1992). The HADCM2 model has a finer resolution of 2.5° latitude \times 3.75° longitude than the other models.

The observed near-surface temperature data are taken from Jones and Briffa (1992). We obtain an estimate of the observed internal variability of climate by subtracting an estimated greenhouse gas signal in the same way as described in Hetal96. The pattern of the subtracted signal is based on the first EOF of the model simulation C, but the time evolution of the pattern amplitude was smoothed by fitting a linear response model that was then forced with the same forcing as in the climate model (and CO_2 observations between 1860 and 1880). The residual, referred to in the following as “VOBS”, should provide a better estimate of the unforced climate variability than the raw observations, but will presumably still be contaminated by the climate response to natural or uncorrected anthropogenic external forcings (volcanic eruptions, changes in solar radiation, aerosol forcing, as well as a possible residual greenhouse warming signal). The VOBS dataset is discussed in Jones and Hegerl (in preparation 1997).

3.5 Construction of the optimal fingerprints

The noise covariance matrix used for constructing the optimized fingerprints from the signal patterns g_c and g_{ab} is estimated from 30-year trend patterns derived from the HAML simulation. The dimension of the full gridpoint space is too high to estimate the noise covariance matrix reliably from the limited amount of data. All data used in the detection and attribution analysis (i.e. the signal guess-patterns, the observed trend patterns and all model trend patterns) are therefore truncated to the same lower dimensional subspace. The dimension of the sub-space

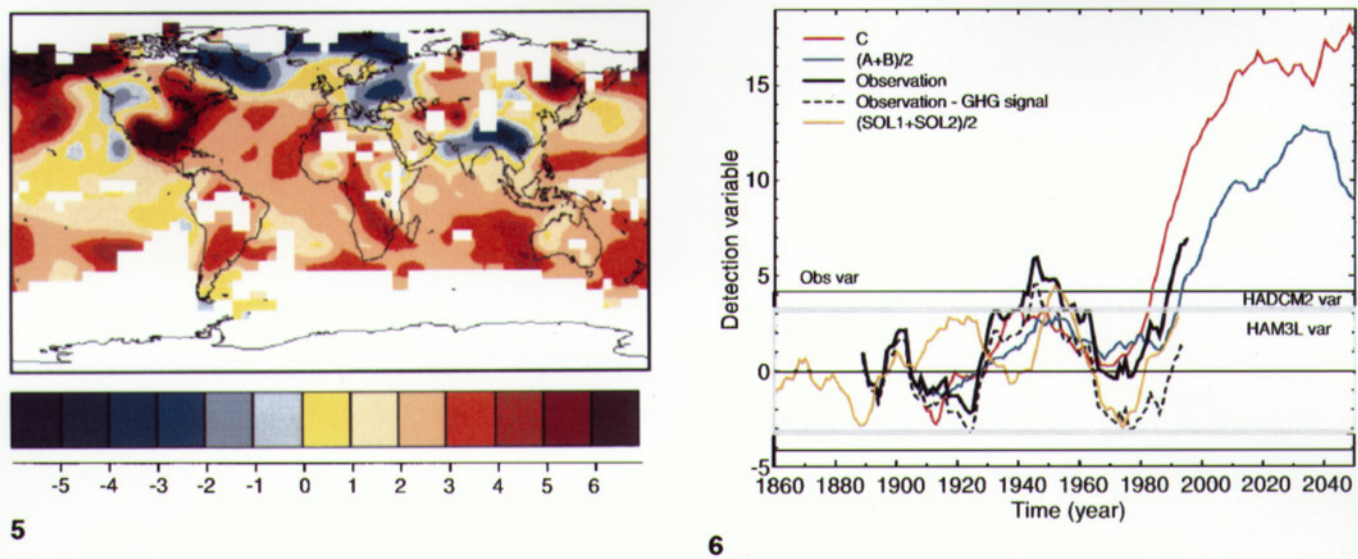


Fig. 5. Optimal fingerprint calculated from the HAML variability data for the greenhouse gas-plus-aerosol climate change signal. The optimal fingerprint shows a cooling in the North Atlantic and changed patterns over the large land masses relative to the climate change pattern (Fig. 3b), but retains the main feature that the warming is weaker in the Northern Hemisphere than in the Southern Hemisphere (normalized in the same way as Fig. 3)

Fig. 6. Evolution of the detection variable (computed with the optimal fingerprint) for 30-y trend patterns from the observations, the average $(A + B)/2$ of the simulations A, B, simulation C and the average of simulations SOL1 and SOL2. The time refers to the final year of the 30-y interval used to compute the trend pattern. 95% confidence intervals derived from four sets of variability data are also indicated (note that the HAM3L and the GFDL confidence limit are very close). For the present one-tailed test (the signal is expected to be positive) the positive confidence limit corresponds to the 97.5% significance level. The recent observed trends exceed this limit, indicating that they represent a significant climate change at the 97.5% confidence level. Also shown are the observations after a model-derived estimate of the evolution of the greenhouse gas signal has been subtracted. The fingerprint is normalized relative to the standard deviation of the HAML noise, the unit value of the detection variable corresponding to the standard deviation of the HAML noise

should be significantly smaller than the effective number of independent realizations of the available data, which determines the rank of the estimated covariance matrix. We chose the first 10 EOFs of the greenhouse gas-plus-aerosol forcing simulation A (for a discussion of the truncation, see Appendix).

Figure 5 shows the optimal fingerprint for the greenhouse gas-plus-aerosol forcing for annual mean near surface temperature (transformed back into gridpoint space). Compared to the original signal guess-pattern (Fig. 3b), the reduced warming south of Greenland is changed to a cooling extending into Northern Europe. The pattern over large land masses is also changed, for example over North America. The optimal fingerprint for the greenhouse gas only signal (not shown) exhibits substantially more warming in northern mid-latitudes than that for the combined forcing. It resembles on the large scale the optimal fingerprint based on the earlier EIN greenhouse warming signal.

4 Results for a single fingerprint

For climate change detection, as opposed to attribution, a single-pattern analysis, as used in Hetal96, is the most effective approach, since the power of a statistical test is the higher the smaller the number of dimensions (see e.g.

Hasselmann 1979). We therefore first carry out a single pattern detection analysis, applying the signal pattern from the mean greenhouse gas-plus-aerosol forcing experiment $(A + B)/2$ in the same way as in Hetal96, to investigate whether the inclusion of anthropogenic aerosol forcing significantly affects the previous detection results. Subsequently, we shall apply the two fingerprints derived from the anthropogenic forcing experiments to address the attribution question and assess which of the three experiments C, $(A + B)/2$ or $(SOL1 + SOL2)/2$, is the most consistent with the observations.

For the detection test, we need to compute the detection variable Eq. (1) from the observations, estimate the variability of the detection variable associated with natural climate variability and assess then the statistical significance of the latest 30-y trends. Technical details of each of these steps are given in Hetal96. Figure 6 shows the time evolution of the computed detection variable $d(t)$ (Eq. 1) obtained by applying the optimal fingerprint derived from the experiment $(A + B)/2$ to the spatial patterns of running 30-y trends $\Psi(t)$ computed from the observations. The fingerprint is normalized with respect to the metric defined by the HAML covariance matrix (Eqs. 3, 4). Also shown for comparison in Fig. 6 are the time evolutions of the detection variables obtained by applying the optimal fingerprint of the $(A + B)/2$ experiment to the running 30-y trends of the climate change simulations $(A + B)/2$,

C and $(\text{SOL1} + \text{SOL2})/2$. The recent rapid increase in the detection variable for the observations agrees quite well with the time evolution of the detection variable computed from the anthropogenic climate change simulations (but is seen also until 1992 in the solar simulation). The detection variable for both anthropogenic climate change simulations stabilizes at a constant level in the first half of the next century, indicating a constant rate of temperature increase at that time.

As expected, the time evolution of the greenhouse gas only simulation C shows an earlier warming than the greenhouse gas-plus-aerosol simulation $(A + B)/2$. (However, the warming also occurs earlier than in the previous EIN greenhouse warming only simulation of Cubasch et al. 1995 used by Hetal96. This must be attributed partly to model changes and a delayed warming in the EIN simulation associated with the experimental setup, Cubasch et al. 1995, partly to statistical natural variability fluctuations, as seen in the Monte Carlo experiments of Cubasch et al. 1994).

Since both predicted signal patterns (Fig. 3a, b) have a strong global mean warming contribution, the detection variables are dominated by the global mean warming trends (see Santer et al. 1993; 1995a; Hetal96, and the figure in Hegerl and North 1997). This explains why the trends from simulation C are not strongly reduced, although the signal pattern for simulation C differs from the assumed signal pattern for simulation $(A + B)/2$. It also explains why the evolution of the detection variable computed for the observations using the greenhouse gas-plus-aerosol fingerprint is quite similar to the earlier results using a greenhouse warming only fingerprint. The distinction between the different forcing hypotheses is better seen using a two-pattern approach, as will be discussed in the next section.

In Fig. 6, the detection variable for the latest observed trend (1966–1995) d computed with the optimal fingerprint f_{ab} for the greenhouse gas-plus-aerosol forcing is seen to exceed the 95% confidence intervals (discussed later) for climate noise, as estimated from three CGCM simulations and observations. Since positive values of the detection variable are expected for anthropogenic climate change, the significance levels can be based on a one-sided test. For this test, the upper limits of the two-sided 95% confidence intervals in Fig. 6 correspond to 97.5% significance limits. Thus we conclude that the latest observed trend (1966–1995) exceeds the 97.5% significance level for an observed climate change signal for all available estimates of natural variability, and that the null hypothesis that the observed temperature trends are natural can be rejected.

The peak warming trends are seen to exceed the estimated 95% confidence intervals of natural variability trends not only in the last decades, but also in the first half of this century. This is consistent with but also a cautionary reminder of the statistical nature of the detection test: the detection variable is expected to exceed the 97.5% one-sided significance level 2.5% of the time also in the absence of a greenhouse gas forcing (see also Barnett et al. 1996, for uncertainties in decadal and secular model variability). But we note the basic distinction between the test for an unusual event at a specified time (namely the last

30 y) and the occurrence of an unusual event at some unspecified time. The computed 30-y trends of a 570 y paleoclimatic record of summer mean temperatures over Northern Hemisphere land confirm that the warming in the early part of this century was indeed an unusual event, yielding the largest 30-y trend in the entire paleoclimatic record (Bradley et al. 1993). Some of this trend may represent an early anthropogenic signal. The observations with the estimated greenhouse gas signal subtracted (dashed line) lie substantially closer to the model internal variability domain. Estimates of solar insolation changes also indicate a possible increase in solar irradiance during this period (see orange line). This suggests that the observed warming in the first half of this century was partly forced (by a small increase in greenhouse gas concentrations, possibly also an increase in solar insolation), partly an extreme event of internal climate variability. The strong warming in the early part of this century will be discussed again later in the context of the 50-y Northern Hemisphere summer trends.

The 95% confidence intervals were estimated independently for each set of climate variability data and are based on the mean square variability $\langle \tilde{d}^2 \rangle$ of the detection variable for 30-y trends computed from these data, assuming normal distributions. The HAML simulation, which was used to estimate the covariance matrix, was excluded, since the non-independence of the optimized fingerprint and the data would have yielded an artificially suppressed value of $\langle \tilde{d}^2 \rangle$ in addition to that model's already rather low variance (Hetal96). In estimating from observational data, gaps in the time series before 1949 were filled by a least-square regression. The estimate of the 95% confidence intervals from the estimated variances of the different variability data sets were corrected for sampling bias of the relatively short time series using Monte Carlo simulations of a Gaussian first-order auto-regressive process with the same time series length and autocorrelation as the data (see Hetal96).

The observations yield higher variability levels than the coupled models, and the model estimates also differ among each other. However, the differences between observed and simulated variances are in fact smaller than the differences in the 95% confidence intervals shown in Fig. 7. This is because the 95% confidence intervals, inferred from the Monte Carlo simulations, are approximately 2.4 times the estimated standard deviation for the relatively short observed times series, as compared to a factor of 2.0–2.1 for the longer model simulations.

For a quantitative estimate of the benefit of using the optimal fingerprint method it is useful to consider the signal-to-noise ratio

$$s/n = \frac{d}{\langle \tilde{d}^2 \rangle^{1/2}} \quad (11)$$

for various alternative definitions of the detection variable. Table 1 lists the signal-to-noise ratios estimated from different sets of variability data and for three different definitions of the detection variable: (a) the global mean (uniform fingerprint); (b) the scalar product of the observations with the signal guess-pattern ($f = g$); and (c) the detection variable computed with the optimal fingerprint

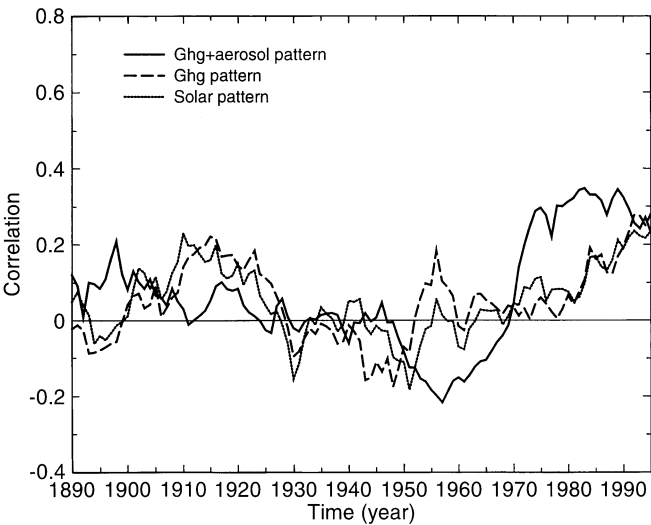


Fig. 7. Centered pattern correlations (with spatial mean subtracted) between observed 30-y trends and the dominant climate change signal for the average (A + B)/2 of the greenhouse gas-plus-aerosol simulations (*solid line*) and the greenhouse gas only simulation C (*dashed line*). Also shown are the correlations of the observed trend patterns with the solar response pattern (*dotted line*; pattern shown in Cubasch et al. 1997)

Table 1. Estimates of the signal-to-noise ratio for the latest observed near surface temperature trends using different fingerprints

	HAML	HAM3	GFDL	HADC	VOBS	ROBS
	L	L		M2		
Mean ^a	6.00	5.14	4.28	3.21	2.99	2.58
Non-optimal ^b	5.92	5.66	4.57	3.35	3.20	2.71
Optimal ^c	(6.92)	4.87^d	4.47^d	4.36	3.40	2.81
Improvement:						
Non-optimal/						
mean	0%	8%	7%	4%	7%	5%
optimal/non-	(17%)	– 20%	– 2%	30%	7%	4%
optimal						

^aMean: a uniform fingerprint yielding the global mean as detection variable;
^bNon-optimal: the signal guess-pattern;
^cOptimal: the optimal fingerprint.

Also listed are the improvements in the signal-to-noise ratios through use of Non-optimal relative to Mean and Optimal relative to Non-optimal. Columns depict the estimates from different variability data: the control simulations HAML, HAM3L, GFDL, HADCM2, and the observations with a previously estimated anthropogenic greenhouse gas signal subtracted (VOBS) and without subtraction of the greenhouse gas component (ROBS). The optimization is performed in a space which is truncated to the first 10 EOFs of simulation A. Here and in the following tables the signal-to-noise ratios using the optimal fingerprint for HAML are given in parentheses, since these have a positive bias due to the use of the same data for the optimization. Bold numbers indicate that the results are significant at the 97.5% level; italics 95%;
^dDenotes a decrease in signal-to-noise ratio due to optimization, indicating problems in the optimization (see Sect. 5)

(Eq. 2). The improvements in the estimated signal-to-noise ratio for the latest observed trend using the signal guess-pattern as fingerprint relative to the straightforward global mean is on the order of 5% for most data, while the

possible further gain from the use of the optimal fingerprint rather than the signal pattern depends strongly on the set of variability data used to estimate $\langle \tilde{d}^2 \rangle$. The standard deviation $\langle \tilde{d}^2 \rangle$ generally decreases when the optimal fingerprint is used (with all fingerprints normalized, Eq. 4, using the unit matrix for the non-optimized case), but as d may also decrease, the signal- to-noise ratio does not necessarily increase in all cases. For example, the standard deviation estimated from 30-y trends of the HADCM2 control simulation using the optimal fingerprint was only slightly smaller than that estimated from the observed variability data when the signal pattern was used as fingerprint, but the variability decreased more in the HADCM2 data than in the observations through use of the optimized fingerprint, leading to a stronger increase in signal-to-noise (s/n) ratio for the HADCM2 data. On the other hand, using the GFDL variability decreased s/n marginally for the optimal fingerprint, while the HAM3L variability data yielded even lower values for the optimized fingerprint.

The differences in the reduction in $\langle \tilde{d}^2 \rangle$ resulting from use of the same optimized fingerprint indicates that the structure of the variability on time scales of several decades is not consistent for the different models. The full potential of the optimal fingerprint approach will presumably be realized only when the models are able to simulate the real climate variability with higher fidelity. However, we should keep in mind that a poor estimate of the noise covariance matrix leading to a “wrong”, i.e. not truly optimal, fingerprint will merely reduce the power of the detection method. This may result in the inability to detect a climate change signal which an accurate fingerprint would have detected, but it will not normally lead to an incorrect detection claim.

We conclude that the reliability of the estimated significance level of the latest observed trends is limited primarily by the reliability of the variability estimates. However, the high signal-to-noise ratios listed in Table 1 provide a cushion against the uncertainties in variability estimates, yielding some confidence in the positive detection result.

5 Application of a two-pattern analysis

While we have shown in the previous section that the latest observed 30-y trend patterns indicate a statistically significant climate change, the cause of this change has not been clearly established. The differences between the detection variable computed from the observations and the values computed from differently forced model simulations are too small compared to the noise to attempt to rank the simulations with respect to their ability to explain the observations. Also, the high values of the detection variable computed from recent trend patterns are mainly due to a strong global mean warming component which is common to all forcing mechanisms, rather than a high similarity between the detailed predicted and observed climate change patterns. Figure 7 shows the centred pattern correlation $r^*(t)$ (after subtraction of the spatial mean) between the observed 30-y trend patterns and the model derived climate change patterns

for anthropogenic climate change. Although the pattern correlation is seen to increase if aerosol forcing is taken into account (see also Santer et al. 1995a, 1996b; Mitchell et al. 1995a; Tett et al. 1996), the results shown in Fig. 7 do not allow a clear distinction between these two forcing hypotheses: The centered pattern correlation between observed 30-y trend patterns and the greenhouse gas only signal pattern or the solar signal pattern (shown in Cubasch et al. 1997) is smaller than the corresponding correlation for the greenhouse gas-plus-aerosol signal pattern for the trends ending between 1970 and 1990, but of the same order of magnitude (~ 0.2 – 0.3) for the latest observed trends. The relatively small values of the correlation agree with other results using seasonal and decadal mean data (Santer et al. 1995a; Mitchell et al. 1995a).

Thus to distinguish between different forcing mechanisms, we need to resort to a multi-fingerprint method as described in Sect. 2. To illustrate the technique we introduce first two fingerprints, corresponding to the greenhouse gas only and greenhouse gas-plus-aerosol forcing cases, for the same annual mean 30-y trends as used in the previous section. Subsequently we consider 50-y northern summer trends, which should be more effective in identifying the aerosol influence.

Since both signal guess patterns contain a strong global mean warming component (Fig. 3a,b), the associated detection variables $\mathbf{d}_c = \mathbf{f}_c^T \cdot \mathbf{\Psi}$, $\mathbf{d}_{ab} = \mathbf{f}_{ab}^T \cdot \mathbf{\Psi}$, (Eq. 1) will be highly correlated. The effect of the aerosol forcing can be better distinguished from the greenhouse gas only forcing if in place of the greenhouse gas-plus-aerosol signal a second signal pattern g_2 is introduced which is orthogonal (with respect to the metric C^{-1} , Eq. 5) to the first greenhouse gas only pattern $g_1 = g_c \cdot R$:

$$g_2 = (g_{ab} - (g_{ab}^T C^{-1} g_1) g_1) \cdot R_2, \quad (12)$$

The normalization factors R are chosen to satisfy the normalization condition (Eq. 3). For the orthonormal signal patterns g_v , the detection variables can be directly equated with the amplitude estimates (Eqs. 8, 9).

Figure 3c shows the statistically orthogonal signal-guess pattern. If the Euclidean metric is used (with the unit matrix substituted for the inverse covariance matrix in Eq. 12), the resultant orthogonal signal pattern g'_2 is qualitatively similar, with a (zonally somewhat more uniform) cooling in the northern mid-latitudes due to higher level of sulfur emissions in this latitude band. However, the Euclidean metric is not the natural metric for the present problem, since the property is lost where the detection variables are identical to the signal amplitudes and uncorrelated.

Figure 8a shows the evolution of the observed running 30-y trend patterns in the two-dimensional phase space spanned by the detection variables d_1 and d_2 . In the orthonormal pattern representation, each point in the phase space represents an amplitude estimate of the greenhouse gas only pattern ($a^1 = d_1$) and the orthogonalized aerosol forcing pattern ($a^2 = d_2$). The combined greenhouse gas-plus-aerosol climate change pattern can be expressed in terms of the pattern $g_c = g_1$ and the aerosol forcing pattern g_2 in the form:

$$g_{ab} = c_1 g_1 + c_2 g_2 \quad (13)$$

by computing the coordinates $c_v = g_{ab}^T C^{-1} g_v$, $v = 1, 2$. The arrow C along the d_1 axis denotes the direction of the greenhouse-gas only signal ($d_2 = 0$) in Fig. 8a, while the arrow AB represents the direction of the greenhouse gas-plus-aerosol signal (as predicted by the model) $d_1/d_2 = c_1/c_2$.

Figure 8a indicates that the latest trend patterns, e.g. the trends 1948–77 until 1966–1995, generally agree more closely with the greenhouse gas-plus-aerosol forcing climate change signal than with the greenhouse gas only signal. To judge the statistical significance of those results, Fig. 8b shows the paths of the detection variable of 30-y trend patterns together with the corresponding climate noise data computed from 30-y trends for different model control simulations and for the observed variability data. The figures clarify the relation between the different single-pattern detection results discussed previously (e.g. Fig. 7). Projection of all data onto the direction AB yields the detection variable and noise distribution for the greenhouse gas-plus-aerosol forcing signal pattern, while projection onto the direction C yields the corresponding result for the greenhouse gas only signal pattern. It is clear from a visual inspection that the detection results for both signal patterns will be rather similar, as the angle between the two pattern directions is rather small. A distinction between the two cases can be made only in the two-dimensional phase space.

Figure 8b also shows the 95% confidence ellipses for two-dimensional Gaussian distributions fitted to the different sets of climate variability. The bias due to sampling, which was estimated using Monte Carlo techniques in the one-dimensional detection test, has not been taken into account in the computation of the two-dimensional confidence areas. Thus we do not show estimates of the confidence ellipses for the relatively short observed time series. For the longer model time series (611 to 1000 y), the ellipsoids can be estimated with some confidence. The percentage of detection variable samples for internal variability which lie outside the respective confidence ellipses is relatively close to 5% for most data (5.3% for GFDL, 6.3% for HADCM2), which suggests that the Gaussian distribution is generally an acceptable approximation. The exceptionally small percentage of detection variables outside the confidence ellipse for HAM3L (2.0%) suggests that these data are influenced either by an outlier in the variability data or a deviation from normality due to model drift. The differences in the noise distributions of the internal variability simulated by the different climate models, as expressed by the confidence ellipses, are clearly larger than can be explained by sampling uncertainty.

As a first test whether the inclusion of aerosols significantly improves the statistical agreement between the observations and the model climate change pattern we consider the signal-to-noise ratio of the second (aerosol) component d_2 for the latest observed trend. If the signal-to-noise ratio is sufficiently high to reject the hypothesis that d_2 represents climate noise only, we conclude that there is a significant aerosol related pattern in the observations. Note that since the orthogonal signal pattern (Fig. 3c) has a spatial mean close to zero, this test is independent of the global mean warming which

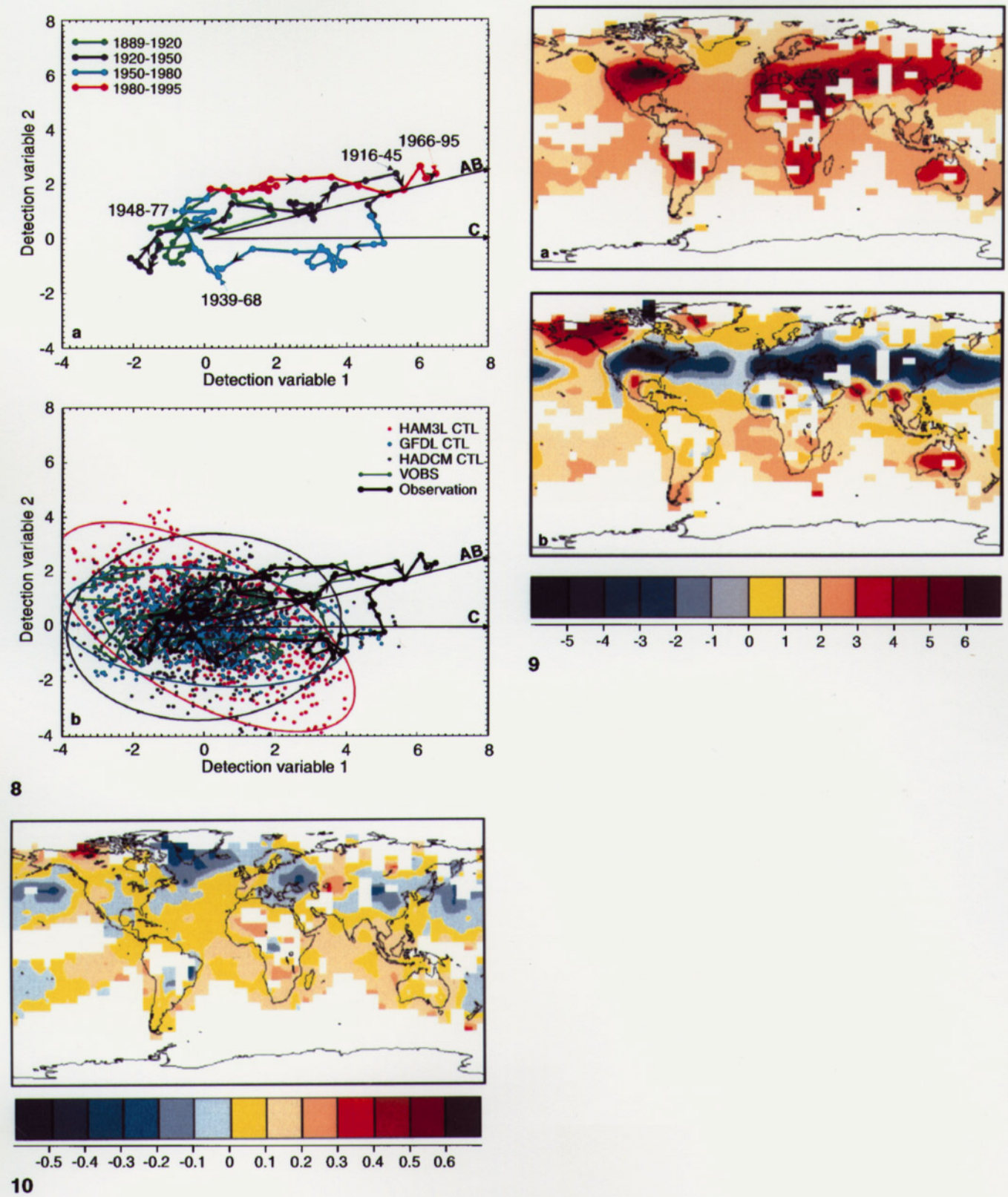


Fig. 8. **a** Evolution of the observed temperature trends in a phase space spanned by (1) the detection variable using the signal pattern for greenhouse warming and (2) the statistically orthogonal signal pattern representing the aerosol effect. The detection variable for trend patterns ending in different time periods are shown in different colors and are also marked in the figure. The arrows show the direction of the time evolution. **b** Shows the results for the observations compared to the detection variables computed with 30-y trend patterns from various climate variability data sets. The 95% confidence ellipses are computed from the detection variable covariances assuming Gaussian distributions

Fig. 9. **a** Signal guess pattern (first EOF) for northern summer (JJA) derived from the greenhouse gas only simulation; **b** orthogonalized pattern derived from the greenhouse gas-plus-aerosol simulation (normalized to the same mean square deviation)

Fig. 10. Observed pattern of 50-y trends (in °C/decade) for the period 1946–1995 in northern summer (JJA; data from Jones and Briffa)

Table 2. Estimates of the signal-to-noise ratio of the detection variable d_2 computed with the component of the greenhouse gas-plus-aerosol pattern which is orthogonal to the greenhouse gas pattern (Fig. 3)

	c_2/c_1^a	HAML	HAM3 L	GFDL	HADC M2	VOBS
Non-optimal	0.32	0.80	0.49	1.09	0.56	0.84
optimal	0.31	(2.32)	1.48	2.60	1.67	1.97

^a c_2/c_1 denotes the ratio of the contributions from the orthogonalized pattern (Fig. 3c) and the greenhouse gas pattern (Fig. 3a) to the greenhouse gas-plus-aerosol climate change pattern (Eq. 13). Bold (italicised) values indicate that the contribution of the aerosol pattern is larger than expected from noise, at the 95 (90)% confidence level. Notation otherwise as in Table 1

dominates the value of d_1 . Since we wish to investigate the consistency of the observations with a greenhouse gas only signal pattern (corresponding to zero values of d_2), unusually high positive or negative signals are relevant. Thus two-sided confidence intervals, as opposed to the previous 1-sided test for single pattern detection, are used. Table 2 shows that d_2 is larger than noise at the 90% confidence level only if the estimate of climate variability is derived from the GFDL control simulation, but is insignificant at this confidence level relative to the HADCM2 and HAM3L noise estimates (a comparison with the noise estimates from the observations with the greenhouse gas signal subtracted is not shown, as this would be biased through a possible residual aerosol signal). The sampling uncertainty in the confidence levels due to the finite length of the time series has been estimated and corrected using Monte Carlo simulations in the same way as for the detection confidence levels. The magnitude of the detection component d_2 in the latest observed trend pattern (and thus the outcome of the consistency test) is sensitive to technical details of the optimization procedure. If the scalar product between the (non-optimized) orthogonal signal pattern and the observations is used to compute d_2 , the resulting value is insignificant relative to all estimates of climate variability (Table 2). The angle between signal patterns (expressed by the ratio c_2/c_1 , Eq. 14) varies with the truncation level and with the variability data used for estimating the covariance matrix (Eq. 5). This implies uncertainties in the computation of the statistically orthogonal signal pattern (i.e. in the form of the ellipses, Fig. 10b). Furthermore, even for the relatively stable c_2/c_1 values in Table 2, the value of d_2 in the observations is sensitive to the analysis parameters. We conclude from the relatively low signal-to-noise ratio, combined with these uncertainties, that the contribution of the aerosol pattern to the observed annual mean 30-y trend patterns cannot at present be convincingly distinguished from noise.

We have also formally applied the attribution test described in Sect. 2 to distinguish if the observed trend patterns are consistent (Eq. 10) with the model values derived for the greenhouse gas only forcing, the greenhouse gas-plus-aerosol forcing and the solar forcing. Again, the results were not fully conclusive: the difference between the observations and the model solar only forced

30-y trends was still within a 90% significance ellipse (although close to the border). The separation between the observations and a greenhouse gas only signal was significant at the 90% level, but as mentioned above this result was sensitive to technical details. The present observed 30-y trends were in relatively good agreement with the model greenhouse gas and aerosol signal. However, we have already mentioned that seasonally stratified data and longer trends should be more suitable for distinguishing between different forcing hypotheses.

6 Results for seasonally stratified data

6.1 Seasonal structure of anthropogenic climate change signals

It may be anticipated that the strongest effect of aerosols will be seen in the Northern Hemispheric summer and autumn. This is confirmed by the studies of Santer et al. (1995a) for simulations using a mixed-layer ocean GCM and Cubasch et al. (1996) for HAM3L model simulations. Thus, we shall focus our seasonal detection and attribution analysis on the (northern) summer. Furthermore, for the reasons stated earlier, we shall consider 50-y rather than 30-y trends. However, before embarking on the specific analysis of a single season, we consider first all four seasons, using as before 30-y trends for better comparison with the annual mean analysis.

The signal guess patterns for seasonal mean data are identified, as in the case of annual means, with the first EOFs computed from each transient global warming simulation. The area with acceptable data coverage is generally smaller for seasonal data (~ 66% of the earth's surface, where a seasonal datapoint is accepted for a grid-box if at least one month is observed) than for the annual mean data (~ 75%, as discussed in Sect. 3, see Fig. 10). The first EOF of the average (A + B)/2 of the two greenhouse gas-plus-aerosol forcing simulations explains approximately 48% of the variance in (northern) winter and spring and 58% in summer and autumn, compared with 73% for the annual mean. For the greenhouse gas only simulation C, the first EOF explains about 80% of the variance in winter and spring and about 85% in summer and autumn, compared to 92% for the annual mean. The higher explained variance for the annual mean data follows from the reduction of the natural variability noise through averaging over the annual cycle, while the relatively larger explained variance in summer and autumn is a consequence of the generally lower noise in those seasons.

Figure 9 shows the signal guess pattern for summer for greenhouse gas only forcing compared to the statistically orthogonal pattern introduced by the additional aerosol forcing (the patterns were computed for the 50-y trends discussed in the following section, but are very similar to the 30-y trend patterns). The greenhouse gas only pattern is very similar to the annual mean pattern, except for a smaller warming in the northern high latitudes. The statistically orthogonal pattern in summer is more zonally homogeneous (and also more similar to the orthogonal signal for summer if the Euclidean metric is used).

The time evolution of the EOF coefficients for seasonal data is very similar to the annual mean case (see Fig. 4). Trends computed from the principal component time series confirm that for trends ending after about 1990, the first EOF captures most the climate change signals in all seasons, the higher EOFs having the appearance of noise with no clear trend. However, prior to this date, EOFs 2 or 3 pick up some of the cooling signal in the 1940s to 1970s, when the aerosol forcing was relatively strong compared with the still rather weak greenhouse gas forcing.

The results for the evolution of the detection variables for the four seasons confirm the previous annual mean results and are thus not given in detail: all seasonal data indicated highly significant values of the recent trend patterns in all seasons. Also, the observations indicate a positive but insignificant aerosol forcing pattern in all seasons except winter. However, the amplitude of the aerosol related pattern cannot be rigorously distinguished from noise in any season. A rather interesting feature of the results using seasonally stratified data was that the robustness of the (single-pattern) detection variable results using the optimal fingerprint varied with the season. The use of the optimal fingerprint yielded rather good results (i.e. an increase in signal-to-noise ratio) for most data for summer and autumn. In contrast, the signal-to-noise ratio decreased (relatively independent of technical details, such as the truncation level, data used for optimization, etc.) in winter and spring when the optimal fingerprints were used. We suspect that the lower-resolution models have difficulty in correctly treating cyclonic wave activity in winter. This suspicion is supported by some improvement in the results obtained when data from the higher resolution HADCM2 model were used for optimization.

6.2 Application of the attribution test to 50-year trends of summer data

As has been mentioned, 30-y trends were chosen for the analysis of the annual mean data in order to focus on the accelerating greenhouse warming predicted by climate models for the most recent decades. However, this choice is not optimal for distinguishing between global warming due to greenhouse gases alone and greenhouse gas-plus-aerosol forcing. Aerosol forcing shows a pronounced fairly linear increase over the last 40–50 y, and we therefore expect that 50-y trends should be more suitable for the attribution issue. This is indicated also by the results of Santer et al. (1995a), who found that in correlations of climate change patterns including the spatial mean, 30-y trends yield the strongest differentiation from natural variability noise, whereas if the spatial mean is removed (and thus the bulk of the warming signal), the residual observed spatial pattern correlates better with the predicted signal if longer trends are considered and the data are seasonally stratified. As the aerosol effect is furthermore expected to be strongest in the northern summer, we shall accordingly focus on 50-y trends in this season.

Figure 10 shows the pattern of the latest observed 50-y trends for the period 1946–1995 for Northern Hemispheric summer, from the data of Jones and Briffa (1992).

The reduced warming or cooling in the Northern Hemisphere is in qualitative agreement with the climate change pattern of the greenhouse gas-plus-aerosol model simulation (see Cubasch et al. 1996). For the detection and attribution analysis, the 50-y trends were analyzed in essentially the same way as the 30-y trends. However, since the sampling uncertainties become larger when longer trends are considered, we augmented the original data from the HADCM2 control run by data from a recently completed extension of the simulation, yielding 976 realizations of each season. At the same time we truncated the representation to a 6-dimensional space prior to optimization rather than a 10-dimensional space, since the 1000 y of HAML data yield proportionally less independent 50-y trends than 30-y trends. Since the first 6 EOFs of the greenhouse gas-plus-aerosol forcing simulation A were insufficient to represent the greenhouse gas only pattern (indicated, for example, by differences in the time evolution of the non-optimized detection variable before and after truncation), the 6th EOF was replaced by the first EOF of the greenhouse gas only simulation (after orthonormalization relative to the first five base vectors), thereby ensuring that the pattern was properly represented.

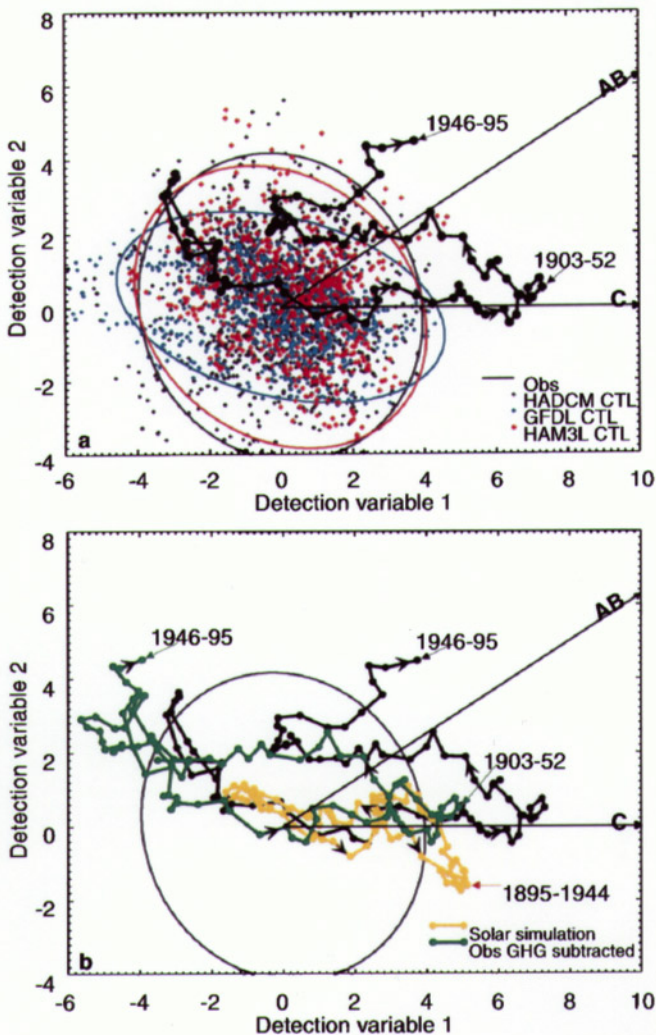
Table 3 lists the signal-to-noise ratios for the detection variable d_2 associated with the aerosol pattern. The most recent 50-y trend has a significantly higher d_2 component than any of the variability data at the 90% confidence level (even at the 95% confidence level for most data). Table 3 also shows that this result is not strongly dependent on the use of optimal fingerprints. The signal-to-noise ratio is nearly as high if the non-optimized signal guess-patterns are used to compute the detection variable. The results using optimal fingerprints show higher signal-to-noise ratios mainly because the fingerprints are better separated, as indicated by the higher ratios of c_2/c_1 (Eq. 14). The relatively similar results of the analysis using the signal-guess patterns indicates that our results are not subject to uncertainty associated with technical details of the optimization (e.g. truncation level).

A further analysis using data over land and ocean separately revealed that both land and ocean contribute to the statistical significance of the aerosol pattern. This can also be anticipated from Figs 9b and 10, which show aerosol induced cooling over both land and ocean in the northern mid-latitudes.

We turn now to the attribution method described in Sect. 2. Here the two-dimensional detection vector is considered to determine whether the observed climate change is consistent with the proposed forcing mechanisms. This involves assessing the difference between the detection

Table 3. Same as Table 2, but for 50-y observed temperature trends of summer data. The contribution of the aerosol pattern is larger than expected from noise in all cases, at the 90 (95)% confidence level for the values printed in italics (bold italics)

Summer, 50y	c_2/c_1	HAML	HAM3L	GFDL	HADCM2
Non-optimal	0.50	3.89	2.25	3.64	<i>1.98</i>
Optimal	0.63	4.49	2.86	4.22	2.53

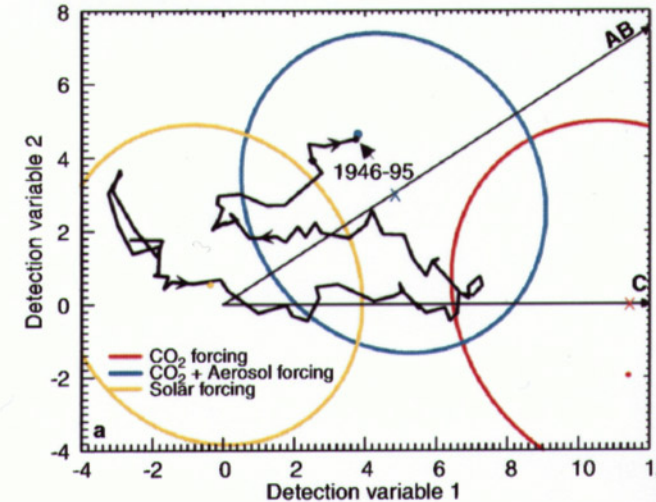


11

Fig. 11. **a** Evolution of observed 50-y northern summer trends in a phase space spanned by the detection variable for the greenhouse gas only and greenhouse gas-plus-aerosol forcing signal patterns, together with various estimates for climate variability (see Fig. 8b) and their associated 95% confidence ellipses. **b** Evolution of observed 50-y northern summer trends, as in a, together with the evolution of the observed trends after subtraction of a computed greenhouse gas component (*green curve*) and the evolution of the simulated trends for the average of the two solar forcing experiments (*orange line*). The relatively strong warming in the early part of the century can be partly attributed to a small greenhouse warming signal (note the weaker observed signal when the greenhouse warming signal is subtracted). Possibly, it may also be partly due to an increase in solar forcing at about this time. The residual trend presumably represents an extreme natural variability event.

Fig. 12. Attribution diagram for the observed 50-year northern summer surface temperature trends. The evolution path of the observed detection vector in phase space is the same as in Fig. 11, the latest trend for the period 1946–1995 being represented by a *large black dot*. The corresponding model predictions and associated 90% confidence ellipses for the difference between the observed and predicted detection vectors are also shown for the three different forcing mechanisms. For the model simulations used to compute the basic signal patterns of the phase space, the confidence ellipses are centered on a projection (denoted by “X”) of the model values for the trend period 1946–1995 (indicated by an appropriately *colored dot*) onto the respective pattern direction, since the noise-free model climate change signal should lie in the this direction (Fig. 3). The detection variable for the latest observed 50-y trend lies inside the confidence ellipse for the combined forcing signal, but outside the confidence ellipse of the greenhouse gas only signal. The observed trend ending in 1992 is also marginally inconsistent with the respective trend of the solar simulation (*orange diamond*). Thus the observations are inconsistent (at a 90% confidence level) with a pure greenhouse gas or solar forced climate change signal but consistent with a greenhouse gas-plus-aerosol climate change signal

vector computed from the most recent observed 50-y summer trends for the years 1946–1995 and the corresponding detection vector predicted by the model simulation using three different forcing mechanisms. If the difference vector lies within a given confidence ellipse determined by the uncertainty in the estimates of the observed and model



12

simulated detection vectors (Eq. 6), the climate change is regarded as consistent (formally not inconsistent) with the proposed mechanism, otherwise the attribution test fails. Figure 11a shows the evolution of the detection vector for the observed 50-y trends in summer in the two-pattern phase space. The figure also shows samples of detection

variables computed from 50-y summer trends based on different climate noise data and the estimated 95% confidence ellipses. The sampling distribution again suggests that the use of a Gaussian distribution is justified, the percentage of climate variability detection variables outside the confidence ellipses lying relatively close to 5% for all data (4% for HAM3L, 3.8% for GFDL and 5.0% for HADCM2). The most recent observed 50-y trend for summer shows a strong contribution of the aerosol related pattern (as discussed for Table 3). This trend also deviates from all estimates of climate variability at the 95% confidence level and thus confirms a significant climate change.

Figure 11a indicates further that the strong trends in the early part of this century agree slightly better with greenhouse only warming than with the greenhouse gas-plus-aerosol forced climate change. These trends are highly exceptional relative to the model internal noise samples. To investigate the origin of these trends, we show in Fig. 11b the detection variables computed from the observations after subtraction of the estimated greenhouse gas forced component (VOBS). As in the annual mean case, this yields a path which lies closer to the model internal variability (as represented by the HADCM2 ellipse), but still represents an exceptionally strong event in this period outside the 95% confidence ellipse. The solar forced simulation again exhibits a trend of similar magnitude around this time. As discussed, this is suggestive of a combination of a forced component and an exceptional variability event in the warming record in the early part of this century. The detection variables for VOBS also lie outside the model noise confidence ellipse for some very early trend patterns (which may be associated with the sparsity of the observations) and for the most recent trends, which resemble a pure aerosol signal (Roeckner et al. 1995).

Figure 12 shows the results of the attribution method for summer 50-y trend patterns. The values of the detection variables computed from simulated trend patterns 1946–1995 are given by coloured dots (for the last trends in the solar simulation, 1943–1992, by a coloured diamond). For the anthropogenic climate change simulation, we prefer to project the detection vectors onto the directions of the signal pattern as defined by the EOFs of the full simulation (see Sect. 2), yielding the coloured crosses. We believe that this definition will provide less noise contaminated estimates of the model signal vectors for the latest trends, at least with respect to the signal directions. However, if the non-modified model trend vectors are used instead, the attribution analysis yields essentially the same results.

The covariance matrix Σ characterizing the confidence ellipse of the difference vector between the observed and model simulated trend signals is given by the sum of the covariance matrix Σ_M of the statistical model signal uncertainty and the corresponding covariance matrix Σ_{obs} of the natural variability noise in the observations (Sect. 2, Eq. 10). The covariance matrix Σ_M estimated from the HAM3L internal variability must be divided by two for the mean greenhouse gas-plus-aerosol simulation $(A + B)/2$ and the solar simulations $(SOL1 + SOL2)/2$ in order to allow for the reduction in uncertainty through averaging over two simulations. Since the internal variability of the HADCM2 model yielded the ellipse with the largest area

(Fig. 11a), we use this model as the most conservative of our estimates of natural climate variability.

The latest observed 50-y summer trend pattern agrees surprisingly well with the model prediction for the greenhouse gas-plus-aerosol simulation, as indicated by the very small signal difference vector in this case. The difference vector lies well within the 90% confidence ellipse. In contrast, the observed trend pattern lies far outside the 90% and the 95% (not shown) confidence ellipse of the greenhouse gas only forced climate change signal. The statistical results listed for the aerosol component d_2 in Table 3 indicate that this statistical inconsistency is found even when only the contribution from the aerosol forcing is considered, disregarding the additional inconsistency arising from the higher predicted mean warming component d_1 in the direction of the greenhouse gas only warming signal.

The observations 1943–1992 (black diamond) lie outside the 90% confidence interval for the solar forcing simulation. The inconsistency in this case is relatively small. However, the increasing amplitude of the global warming component in the observations after 1992 (at a time when the solar insolation rather decreased), and the results of Lean et al. (1995) and Cubasch et al. (1997) support the conclusion that the present observed warming is inconsistent with a purely solar forced climate change.

Our results for the anthropogenic signals are consistent with the results of Santer et al. (1995a). The authors found an increase during the latest decades of the (centred) pattern correlation between the observed and simulated summer and autumn near surface temperatures, where the signal patterns were taken from an equilibrium greenhouse gas-plus-aerosol forcing experiment using a coupled atmosphere-mixed layer ocean model.

We conclude that the latest (1946–1995) 50-y trend of observed near surface summer temperatures is statistically inconsistent with the greenhouse gas only forced climate change simulation at a confidence level higher than 95% and with purely solar forced climate change at a 90% confidence level, while it is highly consistent with the greenhouse gas-plus-aerosol forcing simulation.

7 Discussion and conclusions

In a detection and attribution study of externally forced climate change, we have applied single and multi-fingerprint analyses to observed patterns of 30-y trends of annual mean and 50-y trends of summer near surface temperatures. We used climate change signals derived from five new model simulations, one forced with greenhouse gases only, two with additional (direct) sulphate aerosol forcing, and two forced with hypothesized variations of solar radiation. Using a single fingerprint derived from the average of the two greenhouse gas-plus-aerosol forced climate change simulations, we confirm the result of the previous study of Hetal96 that the latest observed 30-y trend pattern of annual mean data, ending in 1995, can be distinguished from our estimates of natural climate variability at a 97.5% significance level, i.e. the probability of observing a trend which yields values as

high as the observed detection variable due to natural climate variability alone is less than 2.5%.

The latest observed warming trend agrees better, both in terms of pattern and amplitude, with a greenhouse gas-plus-aerosol signal than with a greenhouse gas only signal. The distinction between the three forcing scenarios is best studied in the phase space spanned by the two signal patterns (the signal pattern associated with increases in solar radiation is poorly defined and was thus not used as an additional guess pattern). The two-pattern attribution analysis shows that the observed climate change is consistent with the greenhouse gas-plus-aerosol forced signal computed with the HAM3L model for 30-y annual mean trends and for 50-y trends for (northern) summer, the season with the most pronounced aerosol impact.

On the other hand, the latest observed 50-y summer trend pattern is inconsistent at the 95% confidence level with pure greenhouse gas forcing and at the 90% confidence level with pure solar forcing. Qualitatively similar results were obtained for 30-y trends of annual mean data. In contrast to the results for northern summer, the conclusions in this case were subject to uncertainties associated with technical details of the analysis.

Our investigations indicate that the most effective data filter is generally different for the detection problem, in which the goal is to distinguish between forced climate change and internal climate variability, and the attribution problem, in which the consistency of the climate change signals computed for different candidate forcing mechanisms with an observed and noisy climate change signal is tested. The strongest and most stable signal for climate change detection is found in the 30-y trends of annual mean data. This corresponds to the recent accelerated warming predicted by models. However, the largest difference between pure greenhouse gas and greenhouse gas-plus-aerosol forced climate change appears in the 50-y trends in northern summer. This is consistent with the near linear increase in aerosol forcing since the middle of this century and the stronger impact of aerosols on the radiation balance in the northern summer.

Our results are subject to uncertainties associated with the model-derived climate change signals. Possible systematic errors in the climate model, e.g. errors in the model sensitivity or arising from the residual model drift (whose effect is estimated as small) have not been taken explicitly into account. The time series of the solar insolation changes is highly uncertain. Further uncertainties remain both in the representation of the direct aerosol forcing and in the contribution from the indirect aerosol forcing. The latter has been ignored in our simulations, but is estimated to be of comparable magnitude to the direct forcing. As a test of the impact of uncertainties in the spatial details of the predicted warming pattern, we superimposed a tropical Pacific cooling pattern suggested by Cane et al. (1997) upon the model climate change signal. The results of the detection and attribution analysis were very similar, which increases our confidence that our results are not sensitive to such details.

A further critical aspect of our analysis are the uncertainties in the estimate of climate variability. The climate noise was inferred from observations (after subtraction of

an estimate of the climate change signal) and from the internal variability of different CGCM control simulations. The impact of uncertainties in the natural variability estimates was most apparent in the analysis of the winter and spring seasonal data. The strong dependence of the results on the noise estimates of different models and the failure to systematically increase the signal-to-noise ratio through optimization suggest that for these seasons the structure of the observed multi-decadal climate variability is not correctly reproduced by the different climate models. Such model divergences in the description of the natural climate variability necessarily result in uncertainties in the outcome of all detection and attribution strategies based on pattern oriented methods. The full potential of the optimal fingerprint method will presumably not be realized before these uncertainties are resolved through further model improvements and intercomparison studies.

In addition to uncertainties associated with possible model errors and insufficient data, our results are subject to the fundamental uncertainties of statistics. These are highlighted by the relatively high excursions of the detection variable associated with the warming in the early part of this century. Our results suggest that this warming was caused by an extreme event of natural climate variability, in combination with a small greenhouse warming signal and, possibly, an increase in solar insolation.

These caveats notwithstanding, the signal-to-noise ratio for our detection of a climate change signal in the annual mean 30-y temperature trends is quite high, and largely independent of the details of the optimization and the data used to estimate climate variability. Furthermore, the statistical significance of the inconsistency of the greenhouse gas only signal with the observations found for the 50-y summer trends is also high and quite stable. Thus we have some confidence in our principal conclusions.

We remark finally that our approach to the attribution of a detected significant climate change to different candidate mechanisms is necessarily limited to hypotheses which are specified *a priori* and can be linearly superimposed. However, at present we are not aware of any other convincing explanation of the present climate change.

We conclude from our analysis that the multi-fingerprint method is a useful quantitative approach for the attribution problem of deciding whether an observed climate change signal is consistent, at some prescribed confidence level, with one or a number of competing candidate forcing mechanisms. While a single-pattern analysis yields the result that a significant climate change has been observed which is consistent with either hypothesis of a pure greenhouse gas warming or a greenhouse gas-plus-aerosol forcing, or possibly the third hypothesis of a solar forced climate change, we conclude from a two-pattern analysis that the observed climate change is consistent only with a greenhouse gas-plus-aerosol signal.

Acknowledgements. The authors are grateful to Hans von Storch for support in many aspects of this work, to Henning Rodhe for providing the aerosol forcing data and to Phil Jones for the latest near surface temperature data and for helpful discussions. We also wish to thank Tim Barnett, Lennart Bengtsson, Ben Santer, Uli Schlese,

Ron Stouffer and Simon Tett for support in various aspects of this work. Two reviewers, Myles Allen and Gerald North, provided constructive comments and suggestions. The simulations were carried out at the DKRZ. Different components of the work were sponsored by the Bundesministerium für Bildung, Wissenschaft, Forschung und Technologie (BMBF) through the contract “Klimavariabilität und Signalanalyse”, by the EC Environmental Program under the contract ENV4-CT95-0102 and by NOAA’s Office of Global Program’s Climate Change Data and Detection Program Element, and DOE’s Office of Health and Environmental Research.

Appendix: Implementation of the optimal multi-pattern detection and attribution method

We describe in the following the algorithm used for the numerical implementation of the multi-fingerprint method, including details relevant for the application to the present investigation. The algorithm consisted of the following steps:

1 Prepare data

Choose the set of signal patterns representing the spatial patterns of climate change associated with different forcing mechanisms (using only regions that are reliably simulated and adequately covered by observations, see Fig. 3). We used only a greenhouse gas and a greenhouse gas-plus-aerosol signal pattern, since the solar response pattern could not be sufficiently separated from noise and the greenhouse gas pattern (Cubasch et al. 1996).

Choose a low-dimensional base space which is suitable for representing (1) the climate change signals and (2) the climate variability. We chose the EOFs of the summer/annual mean data of simulation A. The results were essentially the same if the EOFs were computed instead from simulation B, A concatenated with B, or C. We found that for this choice both signal guess patterns (for greenhouse gas only and greenhouse gas-plus-aerosol forcing) were adequately represented, since the non-optimized multi-fingerprint results were not affected qualitatively by a transition from gridpoint space to the truncated space. Using EOFs of the average greenhouse gas-plus-aerosol simulation (A + B)/2 would not have been appropriate, since it would not have fulfilled condition (2), while the use of EOFs from the control simulation (although theoretically more satisfactory) did not fulfil condition (1) at typically chosen truncation levels of up to 12 EOFs.

For summer, the base space was augmented by the first EOF of simulation C, since 6 EOFs of A were unable to adequately represent the greenhouse gas signal pattern (indicated by differences in non-optimized multi-fingerprint results after truncation).

Choose at least two independent sets of data for estimating the climate variability, one for computing the noise covariance matrix (we chose HAML), the others for estimating the statistics of the detection variables (we used four different data sets, VOBS, HAM3L, GFDL, HADCM2).

Choose data for the predicted signal evolution from differently forced climate change simulations. In our case,

we computed trend patterns from model simulations C, (A + B)/2, (SOL1 + SOL2)/2.

2 Determine truncation

The truncation was determined using the same considerations as in Hetal96, which represented a compromise between

- 1. Retaining a sufficient number of degrees of freedom to rotate the signal guess patterns away from noise.
- 2. Avoiding a rotation of the fingerprint into directions representing spurious small scale components with unrealistically low noise levels arising from inadequate sampling.

Figure A1 shows the (uncentred) correlation between the signal-pattern and the optimal fingerprint as a function of the truncation level. The truncation level is chosen as 10, since this is the end of the plateau which we suspect represents the transition region between (1) and (2). We are confident that our results are not sensitive to the chosen truncation level, since small changes in the truncation level did not yield significantly different results, as indicated, for example, by the stable detection results and attribution results for 50-y summer trends. A more rigorous criterion for choosing the truncation level has been suggested by Allen and Tett (1997). The results were also basically insensitive to the substitution of other data in place of the HAML data for the estimation of the noise covariance.

3 Perform the multi-fingerprint analysis

Truncate all data in the same base space chosen in (1) to the truncation level chosen in (2), yielding g_v , $v = 1 \dots p$, Ψ , $\tilde{\Psi}$ and Ψ_s . Estimate the noise covariance matrix from the chosen variability data, yielding C^{-1} , and compute f_v , $v = 1 \dots p$ (Eq. 2), possibly orthogonalizing the fingerprints (Eq. 5).

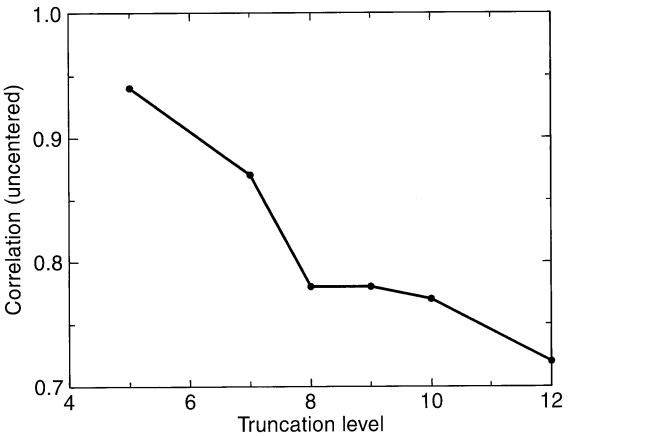


Fig. A1. Uncentered correlation between the guess pattern and the optimal fingerprint as a function of the number of EOFs in a truncated EOF representation

Compute detection variables (Eq. 1) for the observations and the climate change simulations. Compute also detection variables from the variability data in order to estimate the statistics of the detection variables.

Compute the signal-to-noise ratio (Eq. 11) for the detection variable computed for the latest observations and test the null hypothesis that the observations indicate no significant climate change (Sect. 2.1).

Compute the amplitude of each climate change pattern for the observations and model simulations (Eq. 8). Test the consistency between both (Eq. 10, Sect. 2.3).

References

- Allen MR, Tett SFB (1997) Checking for model consistency in optimal fingerprinting. Techn Rep RAL-TR-97040, Rutherford Appleton Laboratory, OX11 0QX, UK
- Barnett TP, Schlesinger ME, Jiang X (1991) On greenhouse gas detection strategies. In: Schlesinger ME (ed) *Greenhouse-gas-induced-climatic change: a critical appraisal of simulations and observations*. Elsevier Science Publishers, Amsterdam, pp 537–558
- Barnett TP, Hasselmann K, North GR, Pennell WT, Rasmussen E (1994) Early detection of induced climate trends: a program of research for detecting the greenhouse effect in the earth's climate. PNL-10241, Pacific Northwest Laboratory, Richland, WA 99352, pp 51
- Barnett TP, Santer BD, Jones PD, Bradley RS, Briffa KR (1996) Estimates of low frequency natural variability in near-surface air temperature. *The Holocene* 6: 255–263
- Bell TL (1986) Theory of optimal weighting of data to detect climatic change. *J Atmos Sci* 43: 1694–1710
- Boucher O, Lohmann U (1995) The sulfate-CCN-cloud albedo effect. A sensitivity study with two general circulation models. *Tellus* 47B: 281–300
- Bradley RS, Jones PD (1993) 'Little Ice Age' summer temperature variations: their nature and relevance to recent global warming trends. *The Holocene* 3: 367–376
- Cane MA, Clement AC, Kaplan A, Kushnir Y, Pozdnyakov D, Seager R, Zebiak SE, Murtugudde R (1997) Twentieth-century sea surface trends. *Science* 275: 957–960
- Crowley TJ, Kim K-Y (1996) Comparison of proxy records of climate change and solar forcing. *Geophys Res Lett* 23: 359–362
- Cubasch U, Hasselmann K, Höck H, Maier-Reimer E, Mikolajewicz U, Santer BD, Sausen R (1992) Time-dependent greenhouse warming computations with a coupled ocean-atmosphere model. *Clim Dyn* 8: 55–69
- Cubasch U, Santer BD, Hellbach A, Hegerl GC, Höck H, Maier-Reimer E, Mikolajewicz U, Stössel A, Voss R (1994) Monte Carlo climate forecasts with a global coupled ocean-atmosphere model. *Clim Dyn* 10: 1–19
- Cubasch U, Hegerl GC, Hellbach A, Höck H, Mikolajewicz Santer BD, Voss R (1995) A climate change simulation starting from 1935. *Clim Dyn* 11: 71–84
- Cubasch U, Hegerl GC, Waszkewitz J (1996) Prediction, detection and regional assessment of anthropogenic climate change. *Geophysica* 32: 77–96
- Cubasch U, Hegerl GC, Voss R, Waszkewitz J, Crowley TJ (1997) Simulation with an OAGCM of the influence of variations of the solar constant on the global climate. *Clim Dyn* accepted for publication
- Earman J (1992) *Bayes or bust? A critical examination of Bayesian confirmation theory*. MIT Press, Cambridge, Mass, 272 pp
- Folland CK, Karl TR, Nicholls N, Nyenzi BS, Parker DE, KYa Vinnikov (1992) Observed climate variability and change, Section C. In: Houghton JT, Callander BA, Varney SK (eds) *Climate change 1992. The supplementary report to the IPCC scientific assessment*. Cambridge University Press, Cambridge, pp 135–170
- Gschwandtner G, Gschwandtner K, Eldrige K, Mann C, Mobley D (1986) Historic Emissions of sulfur and nitrogen oxides in the United States from 1900 to 1980. *J Air Poll Contr Ass* 36: 139–149
- Hasselmann K (1979) On the signal-to-noise problem in atmospheric response studies. In: Shaw BD (ed) *Meteorology over the tropical oceans*, Royal Meteorological Society, Bracknell, Berkshire, England, pp 251–259
- Hasselmann K (1993) Optimal fingerprints for the detection of time dependent climate change. *J Clim* 6: 1957–1971
- Hasselmann K (1997) Multi-pattern fingerprint method for detection and attribution of climate change. *Clim Dyn* 13: 601–611
- Hasselmann K, Bengtsson L, Cubasch U, Hegerl GC, Rodhe H, Roeckner E, von Storch H, Voss R, Waszkewitz J (1995) Detection of anthropogenic climate change using a fingerprint method. MPI report, 168 and Ditlevsen P (ed) *Proc "Modern Dynamical Meteorology"*, Symposium in Honour of Aksel Wiin-Nielsen, ECMWF press 1995: 203–221
- Hegerl GC, North GR (1997) Statistically optimal methods for detecting anthropogenic climate change. *J Clim* 10: 1125–1133
- Hegerl GC, von Storch J, Hasselmann K, Santer BD, Cubasch U, Jones PD (1996) Detecting greenhouse gas induced climate change with an optimal fingerprint method. *J Clim* 9: 2281–2306
- Houghton JT, Jenkins GL, Ephraums JJ (eds) (1990) *Climate change. The IPCC scientific assessment*. Cambridge University Press, Cambridge, 364 pp
- Hoyt DV, Schatten KH (1993) A discussion of plausible solar irradiance variations, 1700–1992. *J Geophys Res* 98: 18 895–18 906
- Johns, TC, Carnell RE, Crossley JF, Gregory JM, Mitchell JFB, Senior CA, Tett SFB, Wood RA (1997) The second Hadley Centre Coupled Model: description, spinup and validation. *Clim Dyn* 13: 103–134
- Jones PD (1994a) Recent warming in global temperature series. *Geophys Res Lett* 21: 1149–1152
- Jones PD (1994b) Hemispheric surface air temperature variations: a reanalysis and an update to 1993. *J Clim* 7: 1794–1802
- Jones PD, Briffa KR (1992) Global surface air temperature variations during the twentieth century: Part 1, spatial, temporal and seasonal details. *The Holocene* 2: 165–179
- Jones A, Roberts DL, Slingo A (1994) A climate model study of the indirect radiative forcing by anthropogenic aerosols. *Nature* 370: 450–453
- Kattenberg A, Giorgi F, Grassl H, Meehl GA, Mitchell JFB, Stouffer R, Tokioka T, Weaver AJ, Wigley TML (1996) Climate models – projections of future climate. In: Houghton et al. (eds) *The IPCC second scientific assessment*. Cambridge University Press, Cambridge, pp 285–357
- Langner J, Rodhe H (1991) A global three-dimensional model of the tropospheric sulfur cycle. *J Atmosph Chem* 13: 225–263
- Lean J, Beer J, Bradley R (1995) Reconstruction of solar irradiance since 1600: implications for climate change. *Geophys Res Lett* 22: 3195–3198
- Leroy S (1997) Detecting Climate signals: Some Bayesian Aspects. *J Clim* (in press)
- Maier-Reimer E, Mikolajewicz U, Hasselmann K (1993) Mean circulation of the Hamburg LSG model and its sensitivity to the thermohaline surface forcing. *J Phys Oceanogr* 23: 731–757
- Manabe S, Stouffer RJ (1993) Century-scale effects of increased atmospheric CO₂ on the ocean-atmosphere system. *Nature* 364: 215–218
- Manabe S, Stouffer RJ (1996) Low frequency variability of surface air temperature in a 1000 year integration of a coupled atmosphere-ocean-land surface model. *J Clim* 9: 376–393
- Mitchell JFB, Johns TJ (1997) On the modification of greenhouse warming by sulphate aerosols. *J Clim* 10: 245–267
- Mitchell JFB, Johns TJ, Gregory JM, Tett SFB (1995a) Transient climate response to increasing sulphate aerosols and greenhouse gases. *Nature* 376: 501–504

- Mitchell JFB, Davis RA, Ingram WJ, Senior CA (1995b) On surface temperature, greenhouse gases and aerosols, models and observations. *J Clim* 10:2364–3286
- Mylona S (1993) Trends of sulphur dioxide emissions, air concentrations and depositions of sulphur in Europe since 1880. Rep EMEP MSC-W 2/93, Norwegian Meteorological Institute, Oslo, Norway
- Nicholls N, Gruza GV, Jouzel J, Karl TR, Ogallo LA, Parker DE (1996) Observed climate variability and change, In: Houghton JT, Meira Filho LG (eds) (1996) *Climate change 1995. The IPCC second scientific assessment*. Cambridge University Press, Cambridge, pp 133–192
- North GR, Kim K-Y (1995) Detection of forced climate signals, part II: simulation results. *J Clim* 8:409–417
- North GR, Stevens MJ (1998) Detecting climate signals in the surface temperature record. *J Clim* (in press)
- North GR, Kim K-Y, Shen SSP, Hardin JW (1995) Detection of forced climate signals, part I: filter theory. *J Clim* 8:401–408
- Parker DE, Jones PD, Folland CK, Bevan A (1994) Interdecadal changes of surface temperature since the late nineteenth century. *J Geophys Res* 99:14 373–14 399
- Penner JE, Charlson RJ, Hales JM, Laulainen NS, Leifer R, Novakov T, Ogred J, Radke LF, Schwartz SE, Travis L (1995) Quantifying and minimizing the uncertainty of climate forcing by anthropogenic aerosols, *Bull Am Meteorol Soc* 75:375–400
- Pepper W, Leggett J, Swanrt R, Wasson J, Edmonds J, Mintzer I (1992) Emission scenarios for the IPCC; an update – assumptions, methodology, and results. Rep IPCC WG1 Secretariate, Bracknell, UK
- Roeckner E, Arpe K, Bengtsson L, Brinkop S, Dümenil L, Esch M, Kirk E, Lunkeit F, Ponater M, Rockel B, Sausen R, Schlese U, Schubert S, Windelband M (1992) Simulation of the present-day climate with the ECHAM model: impact of model physics and resolution. MPI report 93, Max-Planck-Institut für Meteorologie, Bundesstr. 55, 20146 Hamburg, 171 pp
- Roeckner E, Siebert T, Feichter J (1995) Climate response to anthropogenic sulfate forcing simulated with a general circulation model. In: Charlson R, Heintzenberg J (eds) *Aerosol forcing of climate*. John Wiley, Chichester pp 349–362
- Santer BD, Wigley TML, Jones PD (1993) Correlation methods in fingerprint detection studies. *Clim Dyn* 8:265–276
- Santer BD, Taylor KE, Penner JE, Wigley TML, Cubasch U, Jones PD (1995a) Towards the detection and attribution of an anthropogenic effect on climate. *Clim Dyn* 12:77–100
- Santer BD, Mikolajewicz U, Brüggemann W, Cubasch U, Hasselmann K, Höck H, Maier-Reimer E, Wigley TML (1995b) Ocean variability and its influence on the detectability of greenhouse warming signals. *J Geophys Res* 100:10 693–10 725
- Santer BD, Wigley TML, Barnett TP, Anyamba E (1996a) Detection of climate change and attribution of causes. In: J. T. Houghton et al. (eds) *Climate change 1995. The IPCC second scientific assessment*, Cambridge University Press, Cambridge, pp 407–444
- Santer BD, Taylor KE, Wigley TML, Jones PD, Karoly DJ, Mitchell JFB, Oort AH, Penner JE, Ramaswamy V, Schwarzkopf MD, Stouffer RS, Tett SFB (1996b) A search for human influences on the thermal structure in the atmosphere. *Nature* 382:39–46
- Schönwiese CD, Birrong W, Schneider U, Stähle U, Ullrich R (1990) Statistische Analyse des Zusammenhangs säkularer Klimaschwankungen mit externen Einflußgrößen und Zirkulationsparametern unter besonderer Berücksichtigung des Treibhausproblems. Report 84, Inst. Meteorology and Geophysics, University of Frankfurt/M, 260 pp
- von Storch J (1994) Interdecadal variability in a global coupled model. *Tellus* 46A:419–432
- von Storch J, Kharim V, Cubasch U, Hegerl GC, Schriever D, von Storch H, Zorita E (1997) A 1260-year control integration with the coupled ECHAM1/LSG general circulation model. *J Clim* 10:1526–1544
- Stouffer RJ, Manabe S, Vinnikov KY (1994) Model assessment of the role of natural variability in recent global warming. *Nature* 367:634–636
- Tett SFB, Mitchell JFB, Parker DE, Allen MR (1996) Human influence on the atmospheric vertical temperature structure: detection and observations. *Science* 247:1170–1173
- Tett SFB, Johns TC, Mitchell JFB (1997) Global and regional variability in a coupled AOGCM. *Clim Dyn* 13:303–323
- von Storch H, Zwiers F (1998) *Statistical analysis in climate research*, Cambridge University Press (in press)
- Wigley TML, Raper SCB (1990) Natural variability of the climate system and detection of the greenhouse effect. *Nature* 344:324–327